CFHTLenS: combined probe cosmological model comparison using 2D weak gravitational lensing

Martin Kilbinger,[1,2,3,4]⋆ Liping Fu,[5] Catherine Heymans,[6] Fergus Simpson,[6]
Jonathan Benjamin,[7] Thomas Erben,[8] Joachim Harnois-Déraps,[9,10] Henk Hoekstra,[11,12]
Hendrik Hildebrandt,[7,8] Thomas D. Kitching,[6] Yannick Mellier,[1,4] Lance Miller,[13]
Ludovic Van Waerbeke,[7] Karim Benabed,[4] Christopher Bonnett,[14] Jean Coupon,[15]
Michael J. Hudson,[16,17] Konrad Kuijken,[11] Barnaby Rowe,[18,19] Tim Schrabback,[8,11,20]
Elisabetta Semboloni,[11] Sanaz Vafaei[7] and Malin Velander[11,13]

[1]*CEA/Irfu/SAp Saclay, Laboratoire AIM, F-91191 Gif-sur-Yvette, France*
[2]*Excellence Cluster Universe, Boltzmannstr. 2, D-85748 Garching, Germany*
[3]*Universitäts-Sternwarte München, Scheinerstr. 1, D-81679 München, Germany*
[4]*Institut d'Astrophysique de Paris, UMR7095 CNRS, Université Pierre & Marie Curie, 98 bis boulevard Arago, F-75014 Paris, France*
[5]*Key Lab for Astrophysics, Shanghai Normal University, 100 Guilin Road, 200234, Shanghai, China*
[6]*Scottish Universities Physics Alliance, Institute for Astronomy, University of Edinburgh, Royal Observatory, Blackford Hill, Edinburgh EH9 3HJ, UK*
[7]*Department of Physics and Astronomy, University of British Columbia, 6224 Agricultural Road, Vancouver, B.C. V6T 1Z1, Canada*
[8]*Argelander-Institut für Astronomie, Universität Bonn, Auf dem Hügel 71, D-53121 Bonn, Germany*
[9]*Canadian Institute for Theoretical Astrophysics, University of Toronto, M5S 3H8, Ontario, Canada*
[10]*Department of Physics, University of Toronto, M5S 1A7, Ontario, Canada*
[11]*Leiden Observatory, Leiden University, Niels Bohrweg 2, NL-2333 CA Leiden, the Netherlands*
[12]*Department of Physics and Astronomy, University of Victoria, Victoria, BC V8P 5C2, Canada*
[13]*Department of Physics, Oxford University, Keble Road, Oxford OX1 3RH, UK*
[14]*Institut de Ciencies de lEspai, CSIC/IEEC, F. de Ciencies, Torre C5 par-2, E-08193 Barcelona, Spain*
[15]*Institute of Astronomy and Astrophysics, Academia Sinica, PO Box 23-141, Taipei 10617, Taiwan*
[16]*Department of Physics and Astronomy, University of Waterloo, Waterloo, ON, N2L 3G1, Canada*
[17]*Perimeter Institute for Theoretical Physics, 31 Caroline Street N, Waterloo, ON, N2L 1Y5, Canada*
[18]*Department of Physics and Astronomy, University College London, Gower Street, London WC1E 6BT, UK*
[19]*California Institute of Technology, 1200 E California Boulevard, Pasadena, CA 91125, USA*
[20]*Kavli Institute for Particle Astrophysics and Cosmology, Stanford University, 382 Via Pueblo Mall, Stanford, CA 94305-4060, USA*

ABSTRACT

We present cosmological constraints from 2D weak gravitational lensing by the large-scale structure in the Canada–France–Hawaii Telescope Lensing Survey (CFHTLenS) which spans 154 deg^2 in five optical bands. Using accurate photometric redshifts and measured shapes for 4.2 million galaxies between redshifts of 0.2 and 1.3, we compute the 2D cosmic shear correlation function over angular scales ranging between 0.8 and 350 arcmin. Using non-linear models of the dark-matter power spectrum, we constrain cosmological parameters by exploring the parameter space with Population Monte Carlo sampling. The best constraints from lensing alone are obtained for the small-scale density-fluctuations amplitude σ_8 scaled with the total matter density Ω_m. For a flat Λcold dark matter (ΛCDM) model we obtain $\sigma_8(\Omega_m/0.27)^{0.6} = 0.79 \pm 0.03$.

We combine the CFHTLenS data with 7-year *Wilkinson Microwave Anisotropy Probe* (*WMAP*7), baryonic acoustic oscillations (BAO): SDSS-III (BOSS) and a *Hubble Space Telescope* distance-ladder prior on the Hubble constant to get joint constraints. For a flat ΛCDM model, we find $\Omega_m = 0.283 \pm 0.010$ and $\sigma_8 = 0.813 \pm 0.014$. In the case of a curved

⋆ E-mail: martin.kilbinger@cea.fr

wCDM universe, we obtain $\Omega_m = 0.27 \pm 0.03$, $\sigma_8 = 0.83 \pm 0.04$, $w_0 = -1.10 \pm 0.15$ and $\Omega_K = 0.006^{+0.006}_{-0.004}$.

We calculate the Bayesian evidence to compare flat and curved ΛCDM and dark-energy CDM models. From the combination of all four probes, we find models with curvature to be at moderately disfavoured with respect to the flat case. A simple dark-energy model is indistinguishable from ΛCDM. Our results therefore do not necessitate any deviations from the standard cosmological model.

Key words: methods: statistical – cosmological parameters.

1 INTRODUCTION

Weak gravitational lensing is considered to be one of the most powerful tools of cosmology. Its ability to measure both the geometry of the Universe and the growth of structure offers great potential to obtain constraints on dark energy and modified gravity. Moreover, to first order, weak lensing does not rely on the relation between galaxies and dark matter (bias), and is therefore a key probe of the dark universe.

Cosmic shear denotes the distortion of images of distant galaxies due to the continuous deflection of light bundles propagating through the inhomogeneous universe. The induced correlations between shapes of galaxies are directly related to the statistical properties of the total (dark + luminous) large-scale matter distribution. With an estimate of the redshift distribution of the lensed galaxies, theoretical predictions of weak-lensing observables can be tested to obtain constraints on cosmological parameters and models. Recent reviews which also summarize past observational results are Bartelmann & Schneider (2001), Van Waerbeke & Mellier (2003), Munshi et al. (2008), Hoekstra & Jain (2008), Bartelmann (2010).

The Canada–France–Hawaii Telescope Legacy Survey[1] (CFHTLS) is a large imaging survey, offering a unique combination of depth ($i_{AB} \lesssim 24.5$ at 5σ point source limiting magnitude) and area (154 deg^2). It is the largest survey volume over which cosmic shear has ever been measured. This paper presents the first cosmological analysis of the complete CFHT Legacy Survey with weak gravitational lensing. We measure the second-order cosmic shear functions from the Canada–France–Hawaii Telescope Lensing Survey (CFHTLenS),[2] which comprises the final CFHTLS data. Earlier analyses of the CFHTLS used the first data release (T0001) with 4 deg^2 of the Deep survey (Semboloni et al. 2005) and 22 deg^2 of the Wide part of the survey (Hoekstra et al. 2006), followed by the third data release (T0003) comprising 55 deg^2 (Benjamin et al. 2007; Fu et al. 2008, hereafter F08). The T0003 lensing data were subsequently employed in further studies (Doré et al. 2008; Kilbinger et al. 2009; Tereno et al. 2009). Only CFHTLS-Wide i'-band data were used for those lensing analyses, and the redshift distribution was inferred from the photometric redshifts from the Deep survey (Ilbert et al. 2006). Photometric redshifts in the Wide were obtained subsequently with the T0004 release (Coupon et al. 2009). The current series of papers uses the final CFHTLenS data release of 154 deg^2 in the five optical bands u^*, g', r', i', z'. The analysis improved significantly in several ways.

(i) The CFHTLS data have been reanalysed with a new pipeline (Erben et al. 2009, 2013).

(ii) Photometric redshifts have been obtained for each individual galaxy in the lensing catalogue from point spread function (PSF)

homogenized images (Hildebrandt et al. 2012). The accuracy has been verified in detail by an angular cross-correlation technique (Benjamin et al. 2013).

(iii) PSF modelling and galaxy shape measurement have been performed with the forward model-fitting method *lens*fit, which has been thoroughly tested on simulations and improved for CFHTLenS (Miller et al. 2013).

(iv) Systematics tests have been performed in a blind way, to yield unbiased cosmological results (Heymans et al. 2012).

(v) The cosmology-dependent covariance matrix is obtained by a mixture of numerical simulations on small scales and analytical predictions on large scales.

The reliability and accuracy of our photometric redshifts allow for 3D weak lensing analyses. The measurement of the lensing correlations for different redshift combinations allows us to obtain information on the growth of structure (e.g. Hu 1999), and has a great potential to constrain dark energy and modified gravity models (e.g. Albrecht et al. 2006; Uzan 2010). In several companion papers, we perform 3D cosmic shear analyses by splitting up galaxies into redshift bins using correlation function methods presented here (lensing tomography: Benjamin et al. 2013; Simpson et al. 2013, Heymans et al., in preparation).

In this paper, we perform a 2D lensing analysis using a single-redshift distribution. Despite the fact that the redshift information is not used in an optimal way, our analysis has several advantages. First, it yields the highest signal-to-noise ratio (S/N) for a single measurement. This is particularly important on large angular scales, where the S/N is too low to be used for tomography. These large scales probe the linear regime, where non-linear and baryonic effects do not play a role, and one can therefore obtain very robust constraints on cosmology (Semboloni et al. 2011). Secondly, we can include low-redshift galaxies without having to consider intrinsic alignments (IA; Hirata & Seljak 2004). For a broad redshift distribution, IA is expected to be a sub-dominant contribution to the cosmological shear–shear correlation with an expected bias for σ_8 which is well within the statistical uncertainty (Kirk, Bridle & Schneider 2010; Joachimi et al. 2011; Mandelbaum et al. 2011), see also a joint lensing and IA tomography analysis over the full available redshift range (Heymans et al., in preparation). Therefore, despite the fact that a 2D lensing is more limited than tomography, it is less noisy and more immune to primary astrophysical systematics. It is therefore a necessary basic step and puts any further cosmological exploitation of CFHTLenS using more advanced tomographic or full 3D lensing techniques on solid grounds. Such analyses are presented in the CFHTLenS companion papers.

This paper is organized as follows. Section 2 provides the expressions for the second-order lensing observables used in this analysis, both obtained from theoretical predictions and estimated from data. The measured shear functions and covariances are presented in Section 3. Cosmological models and sampling methods are introduced

---

[1] http://www.cfht.hawaii.edu/Science/CFHTLS
[2] http://www.cfhtlens.org

in Section 4. The results on cosmological parameters and models are presented in Section 5, followed by consistency tests in Section 6. The paper is concluded with a discussion in Section 7.

2 WEAK COSMOLOGICAL LENSING

In this section the main relations between second-order weak lensing observables and cosmological quantities are given. See Bartelmann (2010) and Hoekstra & Jain (2008) for recent reviews.

2.1 Theoretical background

Weak lensing by the large-scale structure measures the convergence power spectrum P_κ, which can be related to the total matter power spectrum P_δ via a projection using Limber's equation (Kaiser 1992):

$$P_\kappa(\ell) = \int_0^{\chi_{\mathrm{lim}}} \mathrm{d}\chi\, G^2(\chi)\, P_\delta\left(k = \frac{\ell}{f_K(\chi)}; \chi\right). \tag{1}$$

The projection integral is carried out over comoving distances χ, from the observer out to the limiting distance χ_{lim} of the survey. The lens efficiency G is given by

$$G(\chi) = \frac{3}{2}\left(\frac{H_0}{c}\right)^2 \frac{\Omega_{\mathrm{m}}}{a(\chi)} \int_\chi^{\chi_{\mathrm{lim}}} \mathrm{d}\chi'\, p(\chi')\frac{f_K(\chi' - \chi)}{f_K(\chi')}, \tag{2}$$

where H_0 is the Hubble constant, c the speed of light, Ω_{m} the total matter density and $a(\chi)$ the scale factor at comoving distance χ. The comoving angular distance is denoted with f_K and depends on the curvature K of the Universe;

$$f_K(w) = \begin{cases} K^{-1/2}\sin\left(K^{1/2}w\right) & \text{for } K > 0 \\ w & \text{for } K = 0 \\ (-K)^{-1/2}\sinh\left((-K)^{1/2}w\right) & \text{for } K < 0. \end{cases} \tag{3}$$

The 3D power spectrum is evaluated at the wavenumber $k = \ell/f_K(\chi)$, where ℓ denotes the projected 2D wave mode. The function p represents the weighted distribution of source galaxies.

2.2 Flavours of real-space second-order functions

From an observational point of view, the most direct measurement of weak cosmological lensing is in real space, by using the weak gravitational shear signal as derived from galaxy ellipticity measurements. The two-point shear correlation functions (2PCFs) ξ_+ and ξ_- are estimated in an unbiased way by averaging over pairs of galaxies (Schneider et al. 2002b),

$$\hat{\xi}_\pm(\vartheta) = \frac{\sum_{ij} w_i w_j [\varepsilon_{\mathrm{t}}(\boldsymbol{\vartheta}_i)\,\varepsilon_{\mathrm{t}}(\boldsymbol{\vartheta}_j) \pm \varepsilon_\times(\boldsymbol{\vartheta}_i)\,\varepsilon_\times(\boldsymbol{\vartheta}_j)]}{\sum_{ij} w_i w_j}. \tag{4}$$

The sum is performed over all galaxy pairs (ij) with angular distance $|\boldsymbol{\vartheta}_i - \boldsymbol{\vartheta}_j|$ within some bin around ϑ. With ε_{t} and $\varepsilon_\times$ we denote the tangential and cross-component of the galaxy ellipticity, respectively. The weights w_i are obtained from the *lens*fit shape measurement pipeline (Miller et al. 2013). The 2PCFs are the Hankel transforms of the convergence power spectrum P_κ or, more precisely, of linear combinations of the E- and B-mode spectra, P_{E} and P_{B}, respectively. Namely,

$$\xi_\pm(\vartheta) = \frac{1}{2\pi}\int_0^\infty \mathrm{d}\ell\, \ell\, [P_{\mathrm{E}}(\ell) \pm P_{\mathrm{B}}(\ell)]\, \mathrm{J}_{0,4}(\ell\vartheta), \tag{5}$$

where J_0 and J_4 are the first-kind Bessel functions of order 0 and 4, and correspond to the components ξ_+ and ξ_-, respectively.

It is desirable to obtain observables which only depend on the E mode and B mode, respectively. Weak gravitational lensing, to first order, only gives rise to an E-mode power spectrum and, therefore, a non-detection of the B mode is an important sanity check of the data. To this end, we calculate the following second-order shear quantities which can be derived from the correlation functions: the aperture-mass dispersion $\langle M_{\mathrm{ap}}^2 \rangle$ (Schneider et al. 1998), the shear top-hat rms $\langle |\gamma|^2 \rangle$ (Kaiser 1992), the optimized ring statistic $\mathcal{R}_{\mathrm{E}}$ (Fu & Kilbinger 2010) and Complete Orthogonal Sets of E-/B-mode Integrals (COSEBIs; Schneider, Eifler & Krause 2010). The optimized ring statistic was introduced as a generalization of the so-called ring statistic (Schneider & Kilbinger 2007). The corresponding filter functions have been obtained to maximize the figure-of-merit of Ω_{m} and σ_8 for a CFHTLS-T0003-like survey. We use these functions for CFHTLenS which, despite the larger area, has similar survey characteristics. COSEBIs represent yet another generalization and contain all information about the E- and B-mode weak-lensing field from the shear correlation function on a finite angular range.

Being quantities obtained from the 2PCFs by non-invertible relations, these derived functions do not contain the full information about the convergence power spectrum (Eifler, Kilbinger & Schneider 2008), but separate the E and B mode in a more or less pure way, as will now be described. The derived second-order functions can be written as integrals over the filtered correlation functions. They can be estimated as follows:

$$X_{\mathrm{E,B}} = \frac{1}{2}\sum_i \vartheta_i\, \Delta\vartheta_i\, [F_+(\vartheta_i)\xi_+(\vartheta_i) \pm F_-(\vartheta_i)\xi_-(\vartheta_i)]. \tag{6}$$

Here, $\Delta\vartheta_i$ is the bin width, which can vary with i, for example in the case of logarithmic bins. With suitable filter functions F_+ and F_- (Appendix A), the estimator X_{E} (X_{B}) is sensitive to the E mode (B mode) only. The filter functions are defined for the various second-order observables in Table 1 and Appendix A.

All derived second-order functions are calculated for a family of filter functions. For the aperture-mass dispersion, the optimized ring statistic and the top-hat shear root mean square (rms), these are given for a continuous parameter θ which can be interpreted as the smoothing scale. Here and in the following we will use the notation 'ϑ' as the scale for the 2PCFs, and 'θ' as the smoothing scale for derived functions.

For COSEBIs, the filter functions are a discrete set of functions. The latter exist in two flavours, Lin-COSEBIs and Log-COSEBIs, defined through filter functions $F_\pm$ which are polynomials on linear and logarithmic angular scales, respectively. Here we use Log-COSEBIs, for which many fewer modes are required to capture the same information as Lin-COSEBIs (Schneider, Eifler & Krause 2010; Asgari, Schneider & Simon 2012). See Appendix A for more details.

All of the above functions can be expressed in terms of the convergence power spectrum. The general relation is

$$X_{\mathrm{E,B}} = \frac{1}{2\pi}\int_0^\infty \mathrm{d}\ell\, \ell\, P_{\mathrm{E,B}}(\ell)\hat{U}^2(\ell). \tag{7}$$

The functions $F_\pm$ and $\hat{U}^2$ are Hankel-transform pairs; their relation is given by Crittenden et al. (2002) and Schneider, Van Waerbeke & Mellier (2002a) as

$$F_\pm(x) = \int_0^\infty \mathrm{d}t\, t\, \mathrm{J}_{0,4}(xt)\hat{U}^2(t). \tag{8}$$

Table 1. E- and B-mode separating second-order functions. They are estimated as integrals, or sums in the discrete case, over the 2PCFs $\xi_\pm$ multiplied with the filter functions $F_\pm$ with the formal integration range $[\vartheta_{\min}; \vartheta_{\max}]$ (see equation 6). The argument ϑ denotes the integration variable.

Name	$X_{E, B}$	$F_\pm$ (equation 6)	$\hat{U}$ (equation 7)	$\vartheta_{\min}$	$\vartheta_{\max}$	Reference
Aperture-mass dispersion	$\langle M^2_{\mathrm{ap},\times}\rangle(\theta = \vartheta_{\max}/2)$	$T_\pm(\vartheta/\theta)/\theta^2$ (equation A1)	equation (A2)	0	2θ	Schneider et al. (1998)
Top-hat shear rms	$\langle|\gamma|^2\rangle(\theta)$	$S_\pm(\vartheta/\theta)/\theta^2$ (equation A3)	equation (A4)	0	∞	Kaiser (1992)
Optimized ring statistic	$\mathcal{R}_{E,B}(\theta = \vartheta_{\max})$	$T_\pm(\vartheta)$ (equation A6)	n/a	$\vartheta_{\min}$	$\vartheta_{\max}$	Fu & Kilbinger (2010)
COSEBIs	E_n, B_n	$T^{\log}_{\pm,n}(\vartheta)$ (equation A8)	n/a	$\vartheta_{\min}$	$\vartheta_{\max}$	Schneider et al. (2010)

2.2.1 Finite support

The measured shear correlation function is available only on a finite interval $[\vartheta_{\min}; \vartheta_{\max}]$. The upper limit is given by the finite survey size. We choose 460 arcmin, which is roughly the largest scale for which a sufficient number of galaxy pairs are available on at least three of the four Wide patches.[3] The lower limit comes from the fact that for close galaxy pairs, shapes cannot be measured reliably. For *lens*fit, galaxies with separations smaller than the postage stamp size of 48 pixels $\simeq 9$ arcsec tend to have a shape bias along their connecting direction (Miller et al. 2013). Since this direction is randomly oriented to a very good approximation, we do not have to remove those galaxies altogether; setting a minimum angular separation of $\vartheta_{\min} = 9$ arcsec does avoid the correlation of those pairs. Both galaxies from a close pair can be independently correlated with other, more distant galaxies, for which the close-pair shape bias acts as a second-order effect and can safely be neglected.

If the support of the filter functions F_+ and F_- exceeds the observable range, equation (6) leads to biased results, and a pure E- and B-mode separation is no longer guaranteed.

This is the case for the aperture-mass dispersion and the top-hat shear rms. For the former, only the lower angular limit is problematic and causes leakage of the B mode into the E-mode signal on small smoothing scales. On scales larger than $\theta_{\min} = 5.5$ arcmin however, this leakage is below 1.5 per cent for $\vartheta_{\min} = 9$ arcsec (Kilbinger, Schneider & Eifler 2006). We therefore choose $\theta_{\min} = 5.5$ arcmin to be the smallest smoothing scale for $\langle M^2_{\mathrm{ap}}\rangle(\theta)$. Note that on scales smaller than $\vartheta_{\min}$ we set the correlation function to zero and do not use a theoretical model to extrapolate the data on to this range, to avoid a cosmology-dependent bias.

The B-mode leakage for the top-hat shear rms $\langle|\gamma^2|\rangle$ is a function of both the lower and upper available angular scales. Over our range of scales, the predicted leaked B mode for the 7-year *Wilkinson Microwave Anisotropy Probe* (*WMAP*7) cosmology is nearly constant with a value of 5.3×10^{-7}.

The first pure E-/B-mode separating function for which the corresponding filter functions have finite support was introduced in Schneider & Kilbinger (2007). Following that approach, the optimized ring statistic and COSEBIs were constructed in a similar way to not suffer from an E-/B-mode leakage.

An additional bias arises from the removal of close galaxy pairs in the lensing analysis, as was first reported by Hartlap et al. (2011). As previously discussed, *lens*fit produces a shape bias for galaxies separated by less than 9 arcsec, but this bias is random and the close pairs are therefore used in the analysis, to be correlated with other galaxies at larger distances. That said, for very close blended galaxies, where it is non-trivial to determine if there is one or

two galaxies observed, galaxy shapes cannot even be attempted. These blended pairs are therefore not reliably detected and lost from our analysis. This causes a potential bias, since these galaxies are removed preferentially at low redshift, where galaxy sizes are larger, and from high-density regions compared to voids, because galaxies trace the large-scale structure. From fig. 3 of Hartlap et al. (2011) we infer that the magnitude of this effect is at the per cent level on scales larger than 0.8 arcmin for the 2PCFs.

3 CFHTLENS SHEAR CORRELATION DATA AND COVARIANCE

The CFHTLenS data are described in several companion papers; for a full summary see Heymans et al. (2012). Stringent systematic tests have been performed in Heymans et al. (2012) which flag and remove any data in which significant residual systematics are detected. It is this cleaned sample, spanning ~ 75 per cent of the total CFHTLenS survey area, that we use in this analysis. This corresponds to 129 out of 171 MegaCam pointings. In this paper, we complement those tests by measuring the B mode up to large scales (Section 3.5). Comparing this to the previous analysis of F08 shows the improved quality of the lensing analysis by CFHTLenS.

3.1 Redshift distribution

A detailed study of the reliability of our photometric redshifts, the contaminations between redshift bins and the cosmological implications is performed in Benjamin et al. (2013). This work shows that the true redshift distribution $p(z)$ is well approximated by the sum of the probability distribution functions (PDFs) for all galaxies. The PDFs are output by BPZ (Bayesian Photometric Redshift Estimation; Benítez 2000) as a function of photometric redshift z_p, and have been obtained by Hildebrandt et al. (2012). The resulting $p(z)$ is consistent with the contamination between redshift bins as estimated by an angular cross-correlation analysis (Benjamin et al. 2010). The contamination is relatively low for galaxies selected with $0.2 < z_p < 1.3$, which is confirmed by a galaxy–galaxy–lensing redshift scaling analysis in Heymans et al. (2012). The resulting $p(z)$ is shown in Fig. 1. The mean redshift is $\bar{z} = 0.748$. In contrast, the mean redshift of the best-fitting z_p histogram is biased low with $\bar{z} = 0.69$.

3.2 Angular correlation functions

We calculate the 2PCFs by averaging over pairs of galaxies, using the tree code ATHENA.[4] Galaxies are partitioned into nested branches of a tree, forming rectangular boxes in right ascension α and declination δ. For two branches at angular distance ϑ and box sizes d_i

---

[3] W2 as the smallest patch extends to 400 arcmin, whereas W1 probes scales as large as 685 arcmin.

[4] http://www2.iap.fr/users/kilbinge/athena
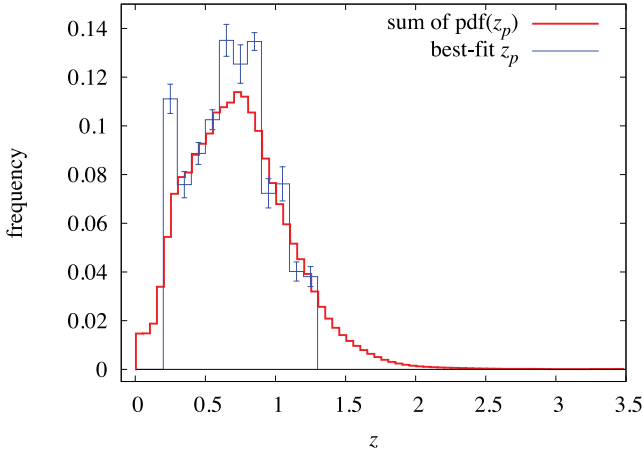
Figure 1. The redshift distribution $p(z_p)$ histogram, estimated as the sum of PDFs for $0.2 < z_p < 1.3$ (thick red curve). For comparison, the histogram of the best-fitting photo-zs is shown as thin blue curve. Error bars correspond to the variance between the four Wide patches.
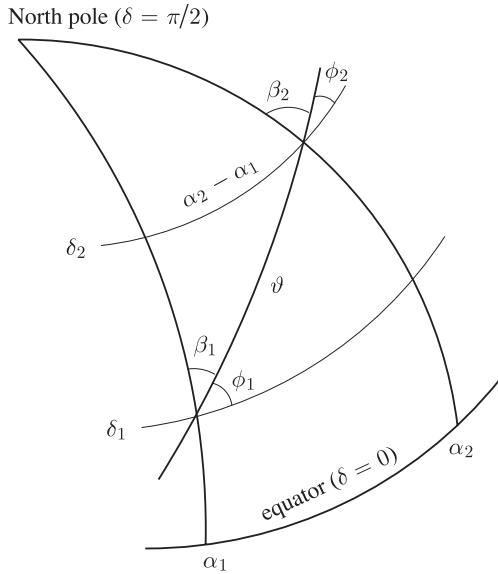
Figure 2. Angles and coordinates on a sphere for two galaxies $i = 1, 2$ located at (α_i, δ_i). Great circle segments are drawn as bold lines.

($i = 1, 2$ along the α and δ direction, respectively) if both opening angles $\omega_i \equiv d_i/\vartheta$ are smaller than a threshold angle ω_{th}, the tree is not followed further down by descending into sub-branches. Instead, the weighted average shear in each branch is used for the 2PCF estimator (equation 4). We found that a value of $\omega_{th} = 0.03$ gives sufficient accuracy compared to the brute-force approach.

We use distances and angles on the sphere to calculate the shear correlation functions, see Fig. 2. For two galaxies $i = 1, 2$ at right ascension and declination (α_i, δ_i), we calculate the great-circle distance ϑ with

$$\cos\vartheta = \cos(\alpha_2 - \alpha_1)\cos\delta_1\cos\delta_2 + \sin\delta_1\sin\delta_2. \tag{9}$$

Each galaxy's ellipticity is measured in a local Cartesian coordinate system with the x-axis going along the line of constant declination and the y-axis pointing to the North pole. We project this ellipticity to the tangential and radial component with respect to the connecting great circle. For that, we calculate the angle β_i between the great circle segments ϑ and α_i. Then, the projection or so-called course

angles are $\phi_i = \pi/2 - \beta_i$. With the sine and cosine rules on the sphere, we get

$$\cos\phi_1 = \frac{\sin(\alpha_2 - \alpha_1)\cos\delta_2}{\sin\vartheta};$$

$$\sin\phi_1 = \frac{\cos\delta_2\sin\delta_1 - \sin\delta_2\cos\delta_1\cos(\alpha_2 - \alpha_1)}{\sin\vartheta}, \tag{10}$$

and corresponding expressions for ϕ_2 by exchanging indices.

To estimate the smoothed second-order quantities, we compute the 2PCFs on 10 000 linear angular bins. This is large enough not to cause a significant E-/B-mode leakage due to the approximation of the integrals over the correlation functions by the direct sum (equation 6). We verified this using CFHTLenS numerical simulations with no B mode (see the next section; see also Becker 2012). We choose the smallest angular distance between two galaxies to be 9 arcsec, corresponding to the first bin centre to be 10.4 arcsec. We calculate the 2PCFs (equation 4) as the weighted mean over the four Wide patches, using the number of galaxy pairs as weight for each bin.
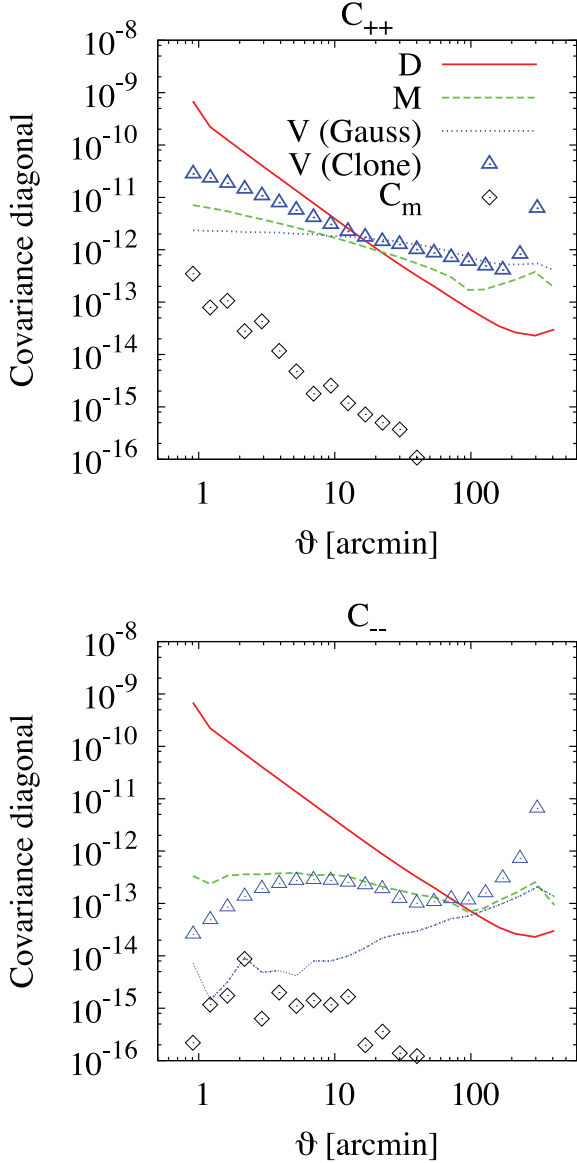
3.3 Data covariance

To model and interpret the observed second-order shear functions, we need to estimate the data covariance and its inverse. The cosmic shear covariance **C** is composed of the shot-noise **D**, which only appears on the diagonal, a cosmic-variance contribution **V**, and a mixed term **M** (Schneider et al. 2002b). The covariance of the 2PCFs comprises four block matrices. The diagonal consists of $\mathbf{C}_{++}$ and $\mathbf{C}_{--}$ which are the auto-correlation covariance matrices of ξ_+ and ξ_-, respectively. The off-diagonal blocks are $\mathbf{C}_{+-}$ and $\mathbf{C}_{-+} = \mathbf{C}_{+-}^t$ which denote the cross-correlation covariance between ξ_+ and ξ_-.

Since the cosmic shear field is non-Gaussian on small and medium angular scales, the cosmic variance involves four-point functions. Neglecting those can yield overly optimistic cosmological constraints (Semboloni et al. 2007, hereafter S07; Takada & Jain 2009; Hilbert, Hartlap & Schneider 2011).

To account for non-Gaussianity, we use N-body simulations from Harnois-Déraps, Vafaei & Van Waerbeke (2012). From these simulations, a 'Clone' of the CFHTLenS data has been produced with the same galaxy redshift distribution, galaxy clustering, masks and noise properties. The cosmological lensing signal is added using ray-tracing through the light cones. The Clone cosmology is a flat Λcold dark matter (ΛCDM) model with $\Omega_m = 0.279$, $\Omega_b = 0.046$, $n_s = 0.96$, $\sigma_8 = 0.817$ and $h = 0.701$. The lensing signal for each galaxy is constructed by ray-shooting through the simulated dark-matter distribution. Each simulated line of sight spans a field of view of 3.5×3.5 deg^2. We fit close to 4×4 MegaCam pointings on each line of sight, which is possible because of overlapping areas between pointings. A total of 184 independent lines of sight are used to calculate the field-to-field covariance matrix. The final matrix is scaled with the ratio of the effective areas (including masks) of 0.11 which corresponds to 90 per cent of the area of 16 MegaCam pointing that fit into each line of sight, divided by 129 MegaCam pointings used in this analysis. We average over three different samples of the galaxy redshift probability distribution, where galaxy redshifts were drawn from the corresponding PDF.

As shown in the upper panel of Fig. 3, the Gaussian prediction for the cosmic variance (Kilbinger & Schneider 2004) for ξ_+ provides a good match to the Clone covariance on intermediate scales, 10 arcmin $\lesssim \vartheta \lesssim 30$ arcmin. On larger scales, up to $\vartheta < 200$ arcmin, the numerical simulations underpredict the power due to the finite box size (e.g. Power & Knebe 2006). Only the last two data points

ance $\mathbf{V}_{\text{cl}}$ to the Gaussian cosmic covariance term $\mathbf{V}_{\text{G}}$. The combined cosmic covariance is

$$V_{ij} = g_{ij}V_{\text{cl},ij} + (1 - g_{ij})V_{\text{G},ij}, \tag{11}$$

where the modulation function g_{ij} alleviates discontinuities in the combined matrix. We choose g_{ij} to be a bi-level step function, with $g_{s,s} = 1/2$; $g_{ij} = 1$ if both indices i, j are smaller than the step index s; and $g_{ij} = 0$ if at least one of the indices i or j is larger than or equal to s. The step index s is chosen such that ϑ_s is the scale closest to 30 arcmin. Equation (11) is applied to all covariances between the two shear correlation functions, i.e. $\mathbf{V}_{++}$, $\mathbf{V}_{+-}$ and $\mathbf{V}_{--}$.

The Clone covariance also contains an additional variance term, which was discovered recently (Sato et al. 2009). This so-called *halo sample variance* (HSV) stems from density fluctuations on scales larger than the (finite) survey size that are correlated with fluctuations on smaller scales. For example, the number of haloes in the survey depends on the large-scale modes outside the survey, since haloes are clustered and do not just follow a Poisson distribution. This introduces an extra variance to the measured power spectrum. The HSV is proportional to the rms density fluctuations at the survey scale (Sato et al. 2009). Since our simulated light-cones are cut-outs from larger boxes of size $L = 147$ Mpc h^{-1} ($L = 231$ Mpc h^{-1}) at redshift below (above) unity, they do contain Fourier scales outside the survey volume and their coupling to smaller scales. The HSV is important on small scales, where our cosmic variance is dominated by the Clone covariance. Following Sato et al. (2009), we estimate the HSV to dominate the CFHTLenS total covariance at $\ell \approx 2 \times 10^3$, corresponding to 5 arcmin which is the Clone covariance regime.

The missing large-scale Fourier modes in the simulation box cause the HSV to be underestimated. A further underestimation comes from the rescaling of the Clone lines of sight to the CFHTLenS area since, in contrast to the other covariance terms, the HSV term decreases less strongly than the inverse survey area (Sato et al. 2009). According to Kayo, Takada & Jain (2013), when naively rescaling from a 25 deg^2-survey to 1500 deg^2, the S/N is too optimistic by not more than 10 per cent. For a re-scaling to the smaller CFHTLenS area, this bias is expected to be much less.

Figure 3. Diagonal of the covariance $\mathbf{C}_{++}$ (top panel) and $\mathbf{C}_{--}$ (bottom), split up into various terms: shot-noise $\mathbf{D}$ (solid red line), mixed term $\mathbf{M}$ (dashed green), cosmic-variance $\mathbf{V}$ (dotted blue line and crosses) and shear calibration covariance $\mathbf{C}_m$ (see Section 3.4).

show an increased variance, which is due to the finite Clone field geometry. When comparing the Clone mean correlation function to a theoretical prediction with cut-off scale $k = (2\pi/147)\, h^{-1}$ Mpc, we get a rough agreement between the two, indicating that the lack of power is indeed caused by the finite box. We draw similar conclusions for the cosmic variance of ξ_-, shown in the lower panel of Fig. 3. Further, we verified that a Jackknife estimate of the variance by sub-dividing the CHFLTenS data into 129 subfields gives consistent results.

3.3.1 Grafting the covariance matrix

We construct the total covariance out to $\vartheta = 350$ arcmin by grafting the Clone covariance $\mathbf{V}_{\text{cl}}$ to the analytical Gaussian prediction. For the latter, we use the method developed in Kilbinger & Schneider (2004), which takes into account the discrete nature of the galaxy distribution and the field geometry. First, we add the Clone covari-

3.3.2 Cosmology-dependent covariance

Our grafted covariance of the 2PCF is estimated for a fiducial cosmological model, which is given by the *N*-body simulations. In order not to bias the likelihood function of the data (Section 4.2) at points other than that fiducial model, we need to account for the fact that the covariance depends on cosmological parameters. We model the cosmology-dependence of the covariance matrix following Eifler, Schneider & Hartlap (2009), who suggested approximative schemes for the mixed term $\mathbf{M}$ and the cosmic-variance term $\mathbf{V}$. Accordingly, for the cosmic-variance term, we assume a quadratic scaling with the shear correlation function. This is true on large scales, where the shear field is close to Gaussian and the covariance is indeed proportional to the square of the correlation function. We calibrate the small-scale Clone covariance in the same way, as any differences in the way the non-Gaussian part might scale are likely to be small.
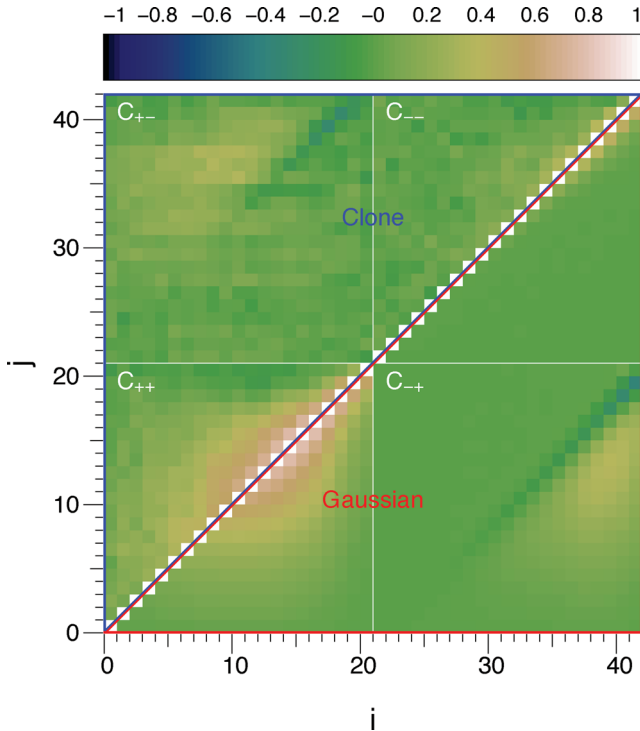
For the mixed term $\mathbf{M}$, we use the fitting formula provided by Eifler et al. (2009). They approximate the variation with Ω_m and σ_8, leaving the matrix fixed for other parameters. The shot-noise term $\mathbf{D}$ does not depend on cosmology. The final expression for the covariance matrix is

$$C_{\mu\nu,ij}(\boldsymbol{p}) = D_i \delta_{ij} \delta_{\mu\nu}$$

$$+ M_{\mu\nu,ij}(\boldsymbol{p}_0) \left(\frac{\Omega_{\rm m}}{0.25} \right)^{\alpha(\mu,\nu,i,j)} \left(\frac{\sigma_8}{0.9} \right)^{\beta(\mu,\nu,i,j)}$$

$$+ V_{\mu\nu,ij}(\boldsymbol{p}_0) \frac{\xi_\mu(\vartheta_i, \boldsymbol{p})}{\xi_\mu(\vartheta_i, \boldsymbol{p}_0)} \frac{\xi_\nu(\vartheta_j, \boldsymbol{p})}{\xi_\nu(\vartheta_j, \boldsymbol{p}_0)}, \qquad (12)$$

where the indices μ, ν stand for the components '+' and '−', and i, j are the angular-scale indices. Here, $\boldsymbol{p} = (\Omega_{\rm m}, \sigma_8, \ldots)$ denotes the cosmological parameter for which the covariance is evaluated, with $\boldsymbol{p}_0$ being the fiducial model of the Clone simulation (Section 3.3). The shot-noise term D_i and the mixed term $M_{\mu\nu,i,j}$ are estimated using the method of Kilbinger & Schneider (2004). The cosmic-variance term $V_{\mu\nu,ij}$ is given in equation (11). The power-law indices α and β depend on the angular scales and the covariance component $(\mu, \nu) \in \{$'+','−'$\}$, and have been obtained in Eifler et al. (2009). We note that the inverse covariance is very sensitive to two apparent outliers of α and β for the $\mathbf{C}_{+-}$-part. To avoid numerical issues, we replace these two numbers by the mean of their neighbouring values. In our case the mixed term of the covariance is important and cannot be neglected (see also Kilbinger & Schneider 2004; Vafaei et al. 2010), in contrast to recent findings by Jee et al. (2012).

During the Monte Carlo sampling (Section 4.2), the covariance is updated at each sample point $\boldsymbol{p}$ using equation (12). We make sure that each calculation of the covariance resulted in a numerically positive-definite matrix, and discard the (rare) sample points for which this is not the case.

In Fig. 4 we show the total covariance $\mathbf{C} = \mathbf{D} + \mathbf{M} + \mathbf{V}$ and compare it to the Gaussian prediction $\mathbf{C}_{\rm G} = \mathbf{D} + \mathbf{M} + \mathbf{V}_{\rm G}$. Both cases are similar on most scales. On small scales the grafted covariance

shows stronger cross-correlations between scales, indicating non-Gaussian effects. We find that the additional covariance $\mathbf{C}_m$ due to the shear calibration (see Section 3.4) can be neglected, as can be seen in Fig. 3 and Section 6.2.

3.3.3 Inverse covariance estimator

It has been shown in Anderson (2003) and Hartlap, Simon & Schneider (2007) that the maximum-likelihood (ML) estimator of the inverse covariance is biased high. The field-to-field covariance from the Clone is such an ML estimate. The bias depends on the number of realizations or fields n, and the number of bins p. The ML estimator can be de-biased by multiplication with the Anderson–Hartlap factor $\alpha = (n - p - 2)/(n - 1)$ (Hartlap et al. 2007).

Our final 2PCF covariance, however, is the mixture of an ML estimate and analytical expressions. The ML estimator is modulated with the Gaussian cosmic variance via equation (11), to which we add the shot-noise and mixed terms, equation (12). We quantify a possible bias of the inverse covariance $(\mathbf{C}_{++})^{-1}$ by varying n for a fixed $p = 10$. For a step index $s = 7$, corresponding to $\vartheta_s = 37$ arcmin, Fig. 5 shows that the trace of $(\mathbf{C}_{++})^{-1}$ does not depend on the ratio p/n for our grafted cosmic covariance matrix. Multiplication with α for $p = 10$ results in an overcorrection, causing a strong decrease of $\mathrm{tr}(\mathbf{C}_{++})^{-1}$ with p/n. A similar albeit less strong decrease is seen when naively taking into account the fact that the Clone covariance only contributes to an effective number of scales $p_{\rm eff} = 6$, according to equation (11) with $s = 7$. The three curves for the inverse seem to converge for $p/n \to 0$. Therefore, we have reason to be confident that any bias of the unaltered inverse of equation (12) is small, and hence we do not need to apply the scalar correction factor α. The addition of a deterministic component to the ML covariance seems to be sufficient to render the estimate of the inverse to be unbiased.
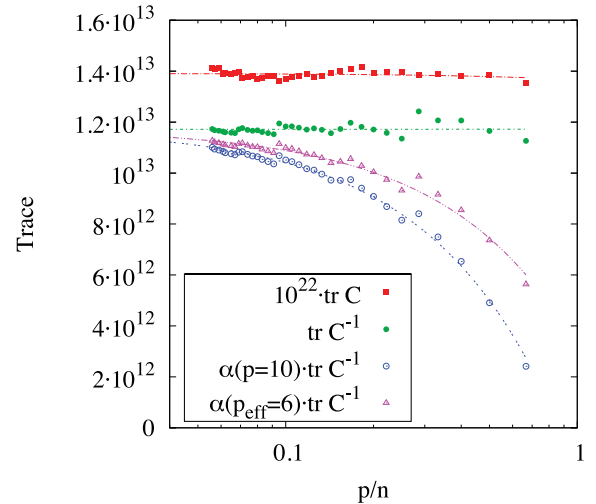

Figure 4. Correlation coefficient of the total covariance, shot-noise plus mixed plus cosmic variance. The lower right triangle (within the red boundary) is the Gaussian prediction; the upper left (blue) triangle shows the total covariance with non-Gaussian parts from the Clone. The four blocks are $\mathbf{C}_{+-}$, $\mathbf{C}_{--}$, $\mathbf{C}_{++}$ and $\mathbf{C}_{-+}$, respectively, as indicated in the plot. The axes labels are the matrix indices i and j.

Figure 5. Trace of the covariance and inverse grafted cosmic covariance, plotted against the ratio of the number of bins p to the number of realizations n. Shown are the cases for covariance (red squares), the inverse (green filled circles) and two cases where the inverse has been multiplied with the Anderson–Hartlap factor α, corresponding to the number of bins $p = 10$ (blue open circles), and $p = 6$ (magenta triangles), causing an overcorrection in both cases. This shows that we can use the inverse covariance estimator without correction (green curve).

3.3.4 Covariance of derived second-order functions

Expressions for the covariance of the derived second-order statistics (equation 6) are straight-forward to obtain, and can be calculated by integrating the covariance of the 2PCFs (Schneider et al. 2002b). However, the necessary precision for the numerical integration requires a large number of angular bins for which the 2PCF covariance has to be calculated, which is very time-consuming. Consequently, for all derived second-order functions we choose not to graft the Clone covariance to the Gaussian covariance, but instead only use the Clone to calculate the total covariance of the derived functions. To include shot noise, we add to each galaxy's shear an intrinsic ellipticity as a Gaussian random variable with zero mean and dispersion $\sigma_\varepsilon = 0.38$. The latter is calculated as $\sigma_\varepsilon^2 = \sum_i \varepsilon_i \varepsilon_i^*$, where the sum goes over all CFHTLenS galaxies in our redshift range. Therefore, the covariance between the 184 Clone lines of sight gives us the total covariance $\mathbf{D} + \mathbf{M} + \mathbf{V}$. Contrary to the case of the 2PCFs (previous section), this covariance stems from a pure ML estimate, and therefore the inverse needs to be de-biased by the Anderson–Hartlap factor α. With a typical number of angular scales of $p = 10$ to 15 the corresponding α is of the order of 0.9. We show that our cosmological results are independent of the number of realisations in Section 6.2. Note that for all the derived estimators, the cosmology-dependence of the covariance is neglected.

For upcoming and future tomographic surveys such as Kilo Degree Survey,[5] Dark Energy Survey,[6] Hyper Suprime-Cam,[7] Euclid[8] (Laureijs et al. 2011) or Large Synoptic Survey Telescope,[9] a much larger suite of simulations will be necessary. The number of realizations n has to be substantially larger than the number of bins p (Hartlap et al. 2007). For a multi-bin tomographic shear survey, p can easily be of the order of several hundreds or more if other probes are jointly measured such as galaxy clustering or magnification. This necessitates on the order of a thousand and more independent lines of sight. This number has to be multiplied by many if a proper treatment of the cosmology-dependence is to be taken into account. Moreover, a simple up-scaling of smaller simulated fields to full survey size might not be easy because of the different area-scaling of the HSV term.

3.4 Ellipticity calibration corrections

We apply the shear calibration as described in Heymans et al. (2012), which accounts for a potential additive shear bias c and multiplicative bias m,

$$\varepsilon^{\text{obs}} = (1 + m)\,\varepsilon^{\text{true}} + c. \tag{13}$$

The additive bias is found to be consistent with zero for ε_1. The second ellipticity component ε_2 shows an S/N and size-dependent bias which we subtract for each galaxy. This represents a correction which is on average at the level of 2×10^{-3}. The multiplicative bias m is modelled as a function of the galaxy S/N and size r. It is fit simultaneously in 20 bins of S/N and r (see Miller et al. 2013). We use the best-fitting function $m(S/N, r)$ and perform the global correction to the shear 2PCFs [see equations (19) and (20) of Miller
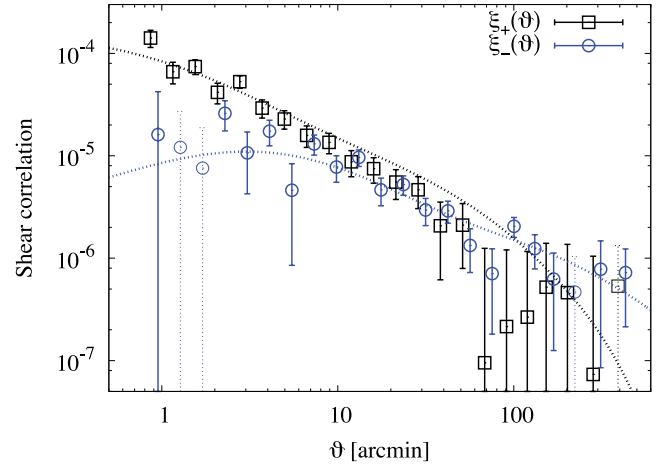
Figure 6. The measured shear correlation functions ξ_+ (black squares) and ξ_- (blue circles), combined from all four Wide patches. The error bars correspond to the total covariance diagonal. Negative values are shown as thin points with dotted error bars. The lines are the theoretical prediction using the *WMAP*7 best-fitting cosmology and the non-linear model described in Section 4.3. The data points and error bars are listed in Table B1.

et al. (2013)]. Accordingly, we calculate the calibration factor $1 + K$ as the weighted correlation function of $1 + m$,

$$1 + K(\vartheta) = \frac{\sum_{ij} w_i w_j (1 + m_i)(1 + m_j)}{\sum_{ij} w_i w_j}. \tag{14}$$

The final calibrated 2PCFs are obtained by dividing ξ_+ and ξ_- by $1 + K$. The amplitude of $1 + K$ is around 0.91 on all scales. The errors on the correlation function from the fit uncertainty are negligible compared to our statistical errors. Furthermore, we calculate the covariance matrix $\mathbf{C}_m$ for the correlation function from this uncertainty, and show in Section 6.2 that the cosmological results remain unchanged by adding this term to the analysis.

Fig. 6 shows the combined and corrected 2PCFs, which are the weighted averages over the four Wide patches with the number of pairs as weights. Note that the data points are strongly correlated, in particular ξ_+ on scales larger than about 10 arcmin. Cosmological results using this data will be presented in Section 5. The correlation signal split up into the contributions from the four Wide patches is plotted in Fig. 7. There is no apparent outlier field. The scatter is larger than suggested by the Poisson noise on large scales, in agreement with the expected cosmic variance.

3.5 E and B modes

The aperture-mass dispersion is shown in the upper panel of Fig. 8. The B mode is consistent with zero on all scales. We quantify this by performing a null χ^2 test, taking into account the B-mode Poisson covariance $\mathbf{C}_\times$ as measured on the Clone,

$$\chi_{\text{B}}^2 = \sum_{ij} \langle M_\times \rangle (\theta_i) \left[\mathbf{C}_\times^{-1} \right]_{ij} \langle M_\times \rangle (\theta_j). \tag{15}$$

Since here the covariance is entirely estimated from the Clone line of sight, the inverse has to be de-biased using the Anderson–Hartlap factor. We consider the B mode over the angular range [5.5; 140] arcmin. As discussed before, the lower scale is where the B mode due to leakage is down to a few per cent. The upper limit is given by the largest scale accessible to the Clone, which is much smaller than the largest CFHTLenS scale: it is 280 arcmin, resulting in an upper limit of $\langle M_{\text{ap}}^2 \rangle$ of half that scale. The resulting
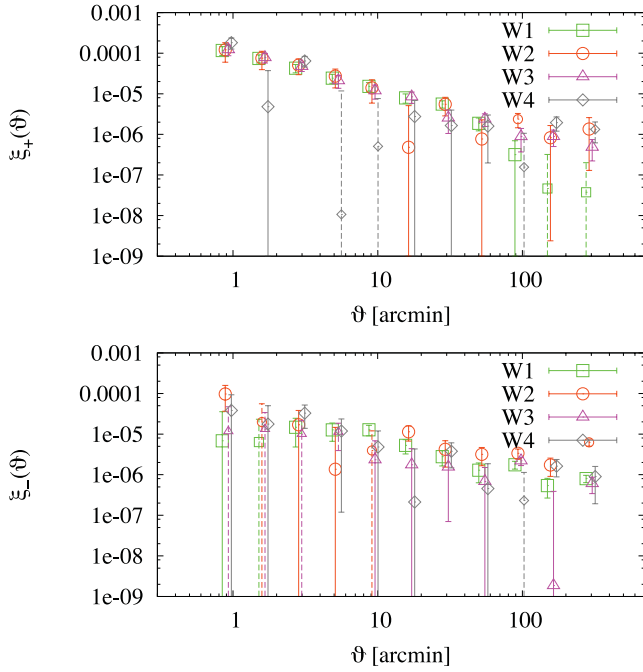
Figure 7. The measured shear correlation functions ξ_+ (top panel) and ξ_- (bottom), for the four Wide patches. The error bars correspond to Poisson noise.

χ^2/degree of freedom (d.o.f.) of $14.9/15 = 0.99$, corresponding to a non-null B-mode probability of 46 per cent. Even if we only take the highest six (positive) data points, we find the χ^2 per d.o.f. to be $\chi^2/\text{d.o.f.} = 4.12/6 = 0.69$, which is less than 1σ significance. The non-zero B-mode signal at around 50–120 arcmin from F08 is not detected here.

The top-hat shear rms B mode is consistent with zero on all measured scales, as shown in the middle panel of Fig. 8. Note, however, that of all second-order functions discussed in this work, $\langle |\gamma|^2 \rangle$ is the one with the highest correlation between data points. The predicted leakage from the B to the E mode is smaller than the measured E mode, but becomes comparable to the latter for $\theta > 100$ arcmin, where the leakage reaches up to 50 per cent of the E mode.

The optimized ring statistic for $\eta = \vartheta_{\min}/\vartheta_{\max} = 1/50$ is plotted in the lower panel of Fig. 8. Each data point shows the E and B modes on the angular range between $\vartheta_{\min}$ and $\vartheta_{\max}$, the latter of which is labelled on the *x*-axis. The B mode is found to be consistent with zero; a χ^2 null test yields a 35 per cent probability of a non-zero B mode.

We first test our calculation of COSEBIs on the CFHTLenS Clone with noise, where we measure a B mode of at most a few $\times 10^{-12}$ for $n \leq 5$ and $\vartheta_{\max} \leq 250$ arcmin. Even though this is a few orders of magnitudes larger than the B mode due to numerical errors from the estimation from theory, it is insignificant compared to the E-mode signal. When including the largest available scales for the Clone however, $\vartheta_{\max} \sim 280$ arcmin, the B mode increases to be of the order of the E mode. This is true independent of the binning or whether noise is added. We presume that this is due to insufficient accuracy with which the shear correlation function is estimated from the simulation on these very large scales, from only a small number of galaxy pairs. Further, for $n > 5$ a similarly large B mode is found for some cases of $(\vartheta_{\min}, \vartheta_{\max})$. Again, the accuracy of the simulations is not sufficient to allow for precise
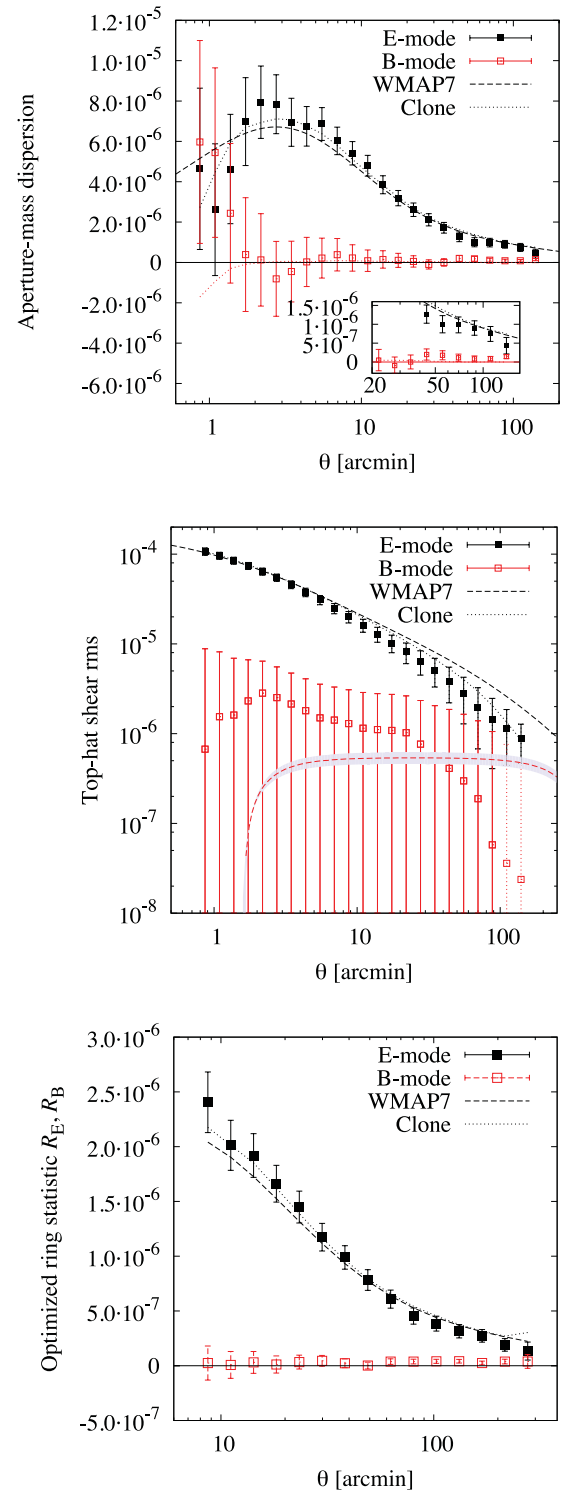
Figure 8. Smoothed second-order functions: aperture-mass dispersion $\langle M_{\text{ap}}^2 \rangle$ (left panel), shear top-hat rms $\langle |\gamma|^2 \rangle$ (middle) and optimized ring statistic $\mathcal{R}_E$ (right), split into the E mode (black filled squares) and B mode (red open squares). The error bars are the Clone field-to-field rms. The dashed line is the theoretical prediction for a *WMAP*7 cosmology (with zero E-/B-mode leakage); the dotted curve shows the Clone lines-of-sight mean E-mode signal. For $\langle M_{\text{ap}}^2 \rangle$ and $\langle |\gamma|^2 \rangle$ the *WMAP*7-prediction of the leaked B mode is shown as red dashed curve; the shaded region in the middle panel corresponds to the 95 per cent *WMAP*7 confidence interval of σ_8 (flat ΛCDM). For the shear top-hat rms, negative points are plotted with dashed error bars.
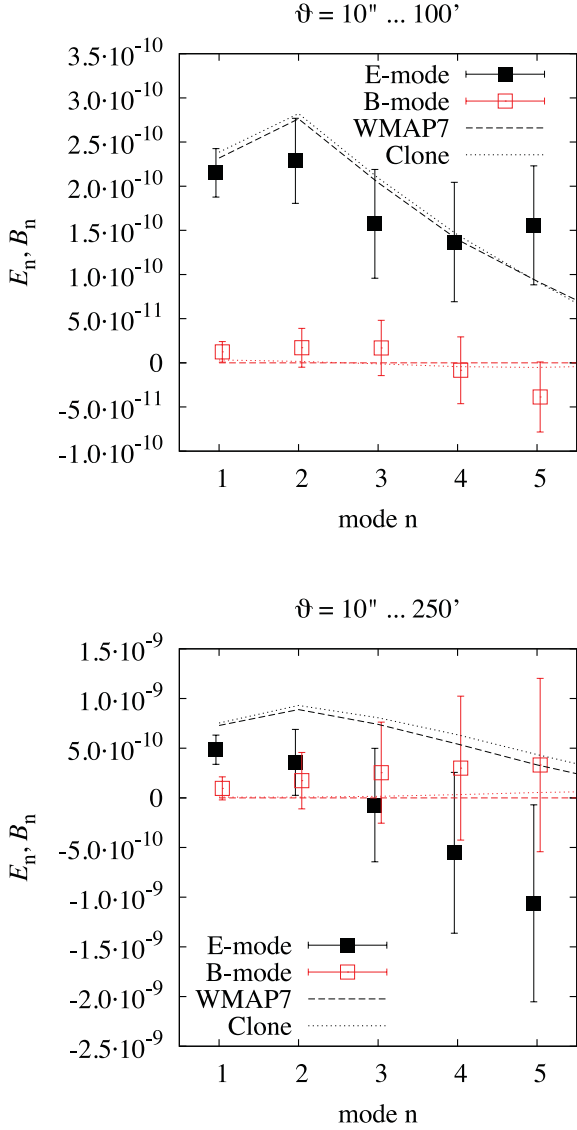
Figure 9. COSEBIs with logarithmic filter functions. The left (right) panel corresponds to a maximum angular scale of 100 arcmin (250 arcmin). The filled (open) squares correspond to the CFHTLenS E mode (B mode). The error bars are the Clone field-to-field rms (rescaled to the CFHTLenS area). The dashed line is the theoretical prediction for a *WMAP*7 cosmology, and the dotted curve shows the Clone mean COSEBIs.

numerical integration over the rapidly oscillating filter functions of Log-COSEBIs for higher modes (Becker 2012). We will therefore restrict ourselves to $n \leq 5$ for the subsequent cosmological analysis.

The measured COSEBIs modes are shown in Fig. 9. We use as smallest scale $\vartheta = 10$ arcsec, and two cases of ϑ_{max} of 100 and 250 arcmin. In both cases we do not see a significant B mode. The S/N of the high mode points decreases when the angular range is increased: for $\vartheta_{max} = 250$ arcmin only the first two modes are significant. This is not unexpected, since the filter functions for $\vartheta_{max} = 250$ arcmin sample larger angular scales and put less weight on small scales where the S/N in the 2PCFs is larger.

A further derived second-order quantity is the shear E-/B-mode correlation functions $\xi_{E, B}$ (Crittenden et al. 2002; Pen, Van Waerbeke & Mellier 2002), which have been used in F08. Whereas they share the inconvenience with the top-hat shear rms of a formal upper

infinite integration limit, they offer no advantage over the latter, and will therefore not be used in this work.

3.6 Conclusion on estimators

We compared various second-order real-space shear functions, starting with the fundamental 2PCFs $\xi_{\pm}$. From the 2PCFs we calculated a number of E-/B-mode separating functions. The top-hat shear rms $\langle |\gamma|^2 \rangle$ is of limited use for cosmological analysis because of the cosmology-dependent E-/B-mode leakage. For the aperture-mass dispersion $\langle M_{ap}^2 \rangle$ this leakage is confined to small scales, whereas the optimized ring statistic $\mathcal{R}_E$ and COSEBIs were introduced to avoid any leakage. The drawback of the 2PCFs is that they are sensitive to large scales outside the survey area and thus may contain an undetectable B-mode signal (Schneider et al. 2010). COSEBIs capture the E-/B-mode signals in an optimal way on a finite angular-scale interval $[\vartheta_{min}; \vartheta_{max}]$. The interpretation of COSEBIs and the matching of modes to angular scales are not straightforward since the corresponding filter functions are strongly oscillating.

For lensing alone, we obtain cosmological parameter constraints on Ω_m and σ_8 for the different estimators discussed in this section. The results and comparisons are presented in Section 5.1.

We decided to use the 2PCFs to compute cosmological constraints in combination with the other probes for the following reasons. The goal of this paper is to explore the largest scales available for lensing in CFHTLenS. This is only possible with a sufficiently large S/N when using the 2PCFs. We note that on these large scales our systematics tests, the star–galaxy shape correlation (Heymans et al. 2012) and the E-/B-mode decomposition (this work) were not possible. However, since both tests have revealed no systematics on smaller scales, we are confident that the shear signal up to very large scales is not significantly contaminated. Moreover, the implementation of a cosmology-dependent covariance is currently only feasible for the 2PCFs.

4 COSMOLOGY SET-UP

4.1 Data sets

We use the following data sets and priors.

(i) *CFHTLenS 2PCFs and covariance as described in Section 3*. We choose the smallest and largest angular bins to be 0.9 and 300 arcmin, respectively. This includes galaxy pairs between 0.8 and 350 arcmin.

(ii) *Cosmic microwave background (CMB) anisotropies*: WMAP7 (Larson et al. 2011; Komatsu et al. 2011). The released *WMAP* code[10] is employed to calculate the likelihood (see also Dunkley et al. 2009). We use camb[11] (Lewis, Challinor & Lasenby 2000) to get the theoretical predictions of CMB temperature and polarization power- and cross-spectra.

(iii) *Baryonic acoustic oscillations (BAO): SDSS-III (BOSS)*. We use the ratio $D_V/r_s = 13.67 \pm 0.22$ of the apparent BAO at $z = 0.57$ to the sound horizon distance, as a Gaussian random variable, from Anderson et al. (2012).

(iv) *Hubble constant*. We add a Gaussian prior for the Hubble constant of $h = 0.742 \pm 0.036$ from Cepheids and nearby Type Ia supernovae distances from *Hubble Space Telescope* (Riess et al. 2009, hereafter R09).

---

[10] http://lambda.gsfc.nasa.gov
[11] http://camb.info

In contrast to Kilbinger et al. (2009) we do not include supernovae of Type (SNIa) Ia. BOSS puts a tight constraint on the expansion history of the Universe, which is in excellent agreement with corresponding constraints using the luminosity distance from the most recent compilation of SNIa (Conley et al. 2011; Suzuki et al. 2012). Both BOSS and SNIa are geometrical probes, and adding SNLS to *WMAP*7+BOSS yields little improvement on cosmological parameter constraints with the exception of w (Sánchez et al. 2012).

All data sets are treated as independent, neglecting any covariance between those probes. Experiments which observe the same area on the sky are certainly correlated since they probe the same cosmological volume. However, this is a second-order effect, like CMB lensing, the integrated Sachs–Wolfe effect (ISW) or the lensing of the baryonic peak (Vallinotto et al. 2007). Compared to the statistical errors of current probes, these correlations can safely be ignored at present, but have to be taken into account for future surveys (Giannantonio et al. 2012).

4.2 Sampling the posterior

To obtain constraints on cosmological parameters, we estimate the posterior density $\pi(\boldsymbol{p}|\boldsymbol{d}, M)$ of a set of parameters $\boldsymbol{p}$, given the data $\boldsymbol{d}$ and a model M. Bayes' theorem links the posterior to the likelihood $L(\boldsymbol{d}|\boldsymbol{p}, M)$, the prior $P(\boldsymbol{p}|M)$ and the evidence $E(\boldsymbol{d}|M)$,

$$\pi(\boldsymbol{p}|\boldsymbol{d}, M) = \frac{L(\boldsymbol{d}|\boldsymbol{p}, M)P(\boldsymbol{p}|M)}{E(\boldsymbol{d}|M)}. \tag{16}$$

To estimate the true, unknown likelihood distribution L, a suite of N-body simulations would be necessary (e.g. Hartlap et al. 2009; Pires et al. 2009). This is not feasible in a high-dimensional parameter space, and for the number of cosmological models probed in this work. Instead, to make progress, we use a Gaussian likelihood function L, despite the fact that neither the shear field nor the second-order shear functions are Gaussian random fields. Nevertheless, this is a reasonable approximation, in particular when CMB is added to lensing (Sato, Ichiki & Takeuchi 2010).

The construction towards the true likelihood function can be informed by further features of the estimators, for example constrained correlation functions (Keitel & Schneider 2011). These constraints are equivalent to the fact that the power spectrum is positive. We do, however, not attempt to make use of these constraints. The expected deviations are minor compared to the statistical uncertainty of the data. The likelihood function is thus given as

$$
\begin{aligned}
L(\boldsymbol{d}|\boldsymbol{p}, M) = \ & (2\pi)^{-m/2}|\mathbf{C}(\boldsymbol{p}, M)|^{-1/2} \\
& \times \exp\left[(\boldsymbol{d} - \boldsymbol{y}(\boldsymbol{p}, M))^{\mathrm{t}}\, \mathbf{C}^{-1}(\boldsymbol{p}, M)(\boldsymbol{d} - \boldsymbol{y}(\boldsymbol{p}, M))\right],
\end{aligned} \tag{17}
$$

where $\boldsymbol{y}(\boldsymbol{p}, M)$ denotes the theoretical prediction for the data $\boldsymbol{d}$ for a given m-dimensional parameter vector $\boldsymbol{p}$ and model M.

We sample the posterior with Population Monte Carlo (PMC; Wraith et al. 2009; Kilbinger et al. 2010), using the publicly available code COSMO_PMC[12] (Kilbinger et al. 2011). PMC is an adaptive importance-sampling technique (Cappé et al. 2004, 2008) in which samples $\boldsymbol{p}_n, n = 1 \ldots N$ are created under an importance function, or proposal density q. The sample can be used as an estimator of

the posterior density π, if each point is weighted by the normalized importance weight

$$\bar{w}_n \propto \frac{\pi(\boldsymbol{p}_n)}{q(\boldsymbol{p}_n)}; \qquad \sum_{n=1}^{N} \bar{w}_n = 1. \tag{18}$$

The main difficulty for importance sampling is to find a suitable importance function. PMC remedies this problem by creating an iterative series of functions $q_t, t = 1, \ldots, T$. In each subsequent iteration, the importance function is a better representation of the posterior, so the distribution of importance weights gets progressively narrower. A measure for this quality of the importance sample is the normalized Shannon information criterion,

$$H_{\mathrm{N}} = -\sum_{n=1}^{N} \bar{w}_n \log \bar{w}_n. \tag{19}$$

As a stopping criterion for the PMC iterations, we use the related *perplexity p*,

$$p = \exp(H_{\mathrm{N}})/N, \tag{20}$$

which lies between 0 and 1, where 1 corresponds to maximum agreement between importance function and posterior.

Most PMC runs reach values of $p > 0.7$ after 10 or 15 iterations. To obtain a larger final sample, we either perform a last importance run with five times the number of points, sampled under the final importance function, or we combine the PMC samples with the five highest values of p. In each iteration we created 10k sample points; the final sample therefore has 50k points.

An estimate $\hat{E}$ of the Bayesian evidence

$$E = \int \mathrm{d}^m p\, L(\boldsymbol{d}|\boldsymbol{p}, M)P(\boldsymbol{p}|M) \tag{21}$$

is obtained at no further computing cost from a PMC simulation (Kilbinger et al. 2010),

$$\hat{E} = \frac{1}{N} \sum_{n=1}^{N} w_n. \tag{22}$$

4.3 Theoretical models

We compare the measured second-order shear functions to nonlinear models of the large-scale structure, with a prediction of the density power spectrum from the HALOFIT fitting formulae of Smith et al. (2003). For dark-energy models, we adopt the scheme of the ICOSMO[13] code (Refregier et al. 2011), which uses the open-CDM fitting formula for a model with $w_0 = -1/3$, and interpolates between this case and ΛCDM for models with differing w_0. This scheme was employed in Schrabback et al. (2010) who compared their nonlinear power spectrum with McDonald, Trac & Contaldi (2006) and found good agreement in the range $w_0 \in [-1.5; -0.5]$ out to k of a few inverse Mpc in the relevant redshift range. Vanderveld et al. (2012) have shown that for ΛCDM the halofit accuracy of 5 to 10 per cent is sufficient for current surveys. From hydro-dynamical simulations, baryonic effects have been quantified. The results depend on the scenario and specific baryonic processes included in the simulations. The bias in the power spectrum to k of few inverse Mpc is between 10 and 20 per cent. The resulting bias on cosmological parameters is smaller than the CFHTLenS statistical errors

---

[12] www.cosmopmc.info

[13] www.icosmo.org

Table 2. Constraints from CFHTLenS orthogonal to the $\Omega_{\rm m}-\sigma_8$ degeneracy direction, using the 2PCF. The errors are 68 per cent confidence intervals. The four columns correspond to the four different models.

Parameter	Flat ΛCDM	Flat wCDM	Curved ΛCDM	Curved wCDM
$\sigma_8 \, (\Omega_{\rm m}/0.27)^\alpha$	0.79 ± 0.03	$0.79^{+0.07}_{-0.06}$	$0.80^{+0.05}_{-0.07}$	$0.82^{+0.05}_{-0.07}$
α	0.59 ± 0.02	0.59 ± 0.03	0.61 ± 0.02	0.61 ± 0.03

(Jing et al. 2006; Rudd, Zentner & Kravtsov 2008; Semboloni et al. 2011).

We also see a good agreement with the ΛCDM simulations of Harnois-Déraps et al. (2012). A more accurate non-linear power spectrum on a wider range of cosmological parameters could be obtained from the Coyote emulator[14] (Heitmann et al. 2009, 2010; Lawrence et al. 2010). Unfortunately, it is limited in wave mode ($k < 2.4$ Mpc) and, more importantly, by an upper redshift of $z = 1$. Due to the scatter in photometric redshifts, we would have to cut at a very low redshift to limit the redshift tail at $z > 1$. For example, with $z_{\rm ph} \leq 0.8$, the fraction of galaxies at $z > 1$ is 5 per cent, and ignoring these galaxies would bias low the mean redshift by 0.05 which would result in a bias on σ_8 which is larger than the uncertainty in the halofit prescription. Alternatively, the hybrid approach of Eifler (2011) could be taken, which pastes the HALOFIT power spectrum to the Coyote emulator outside the k- and z-validity range of the latter. However, this implies multiplying one of the spectra by a constant to make the combined power spectrum continuous, We do not deem this sufficiently justified, since this multiplicative factor does not stem from a fit to numerical simulations and might introduce a bias to σ_8.

We individually run PMC for CFHTLenS and *WMAP*7, respectively. For the combined posterior results, we perform an importance sampling of the *WMAP*7 final PMC sample, multiplying each sample point with the CFHTLenS posterior probability.

For weak lensing only, the base parameter vector for the flat ΛCDM model is $\boldsymbol{p} = (\Omega_{\rm m}, \sigma_8, \Omega_{\rm b}, n_{\rm s}, h)$. It is complemented by w_0 and $\Omega_{\rm de}$ for dark-energy and non-flat models, respectively. With CMB, we add the reionization optical depth τ and the Sunyaev–Zel'dovich (SZ) template amplitude $A_{\rm SZ}$ to the parameter vector. Moreover, we use $\Delta_{\mathcal{R}}^2$ as the primary normalization parameter, and calculate σ_8 as a derived parameter. We use flat priors throughout which, when *WMAP*7 is added to CFHTLenS, cover the high-density regions and the tails of the posterior distribution well.

For model comparison, we limit the parameter ranges to physically well-motivated priors for those parameters which vary between models. This is important for any interpretation of the Bayesian evidence, since the evidence directly depends on the prior. The prior is an inherent part of the model, and we want to compare physically well-defined models.

Thus, we limit the total matter and dark-energy densities $\Omega_{\rm m}$ and $\Omega_{\rm de} \in [0; 1]$, setting a lower physical limit, and creating a symmetrical prior for the curvature $\Omega_{\rm K}$ of $[-1; 1]$, which is bound from below by the physical limit of an empty universe. Note that by sampling both $\Omega_{\rm m}$ and $\Omega_{\rm de}$, the curvature prior is no longer uniform but has triangular shape.

For the model comparison cases we limit w_0 to $[-1; -1/3]$, therefore excluding phantom energy and dark-energy models which are non-accelerating at the present time. These priors are the same as

for the models that were compared using the Bayesian evidence in Kilbinger et al. (2010). The prior ranges for the other parameters are $\Omega_{\rm b} \in [0; 0.1]$, $\tau \in [0.04; 0.2]$, $n_{\rm s} \in [0.7; 1.2]$, $10^9 \Delta_{\mathcal{R}}^2 \in [1.8; 3.5]$, $h \in [0.4; 1.2]$ and $A_{\rm SZ} \in [0; 2]$. For the dark-energy model runs for parameter estimation, which are not used for model comparison, we use a wide prior on w_0 which runs between -3.5 and 0.5.

5 COSMOLOGICAL RESULTS

The most interesting constraints from 2D weak lensing alone are obtained for $\Omega_{\rm m}$ and σ_8, which we discuss below for the four cosmologies considered here. Table 2 shows constraints from lensing alone on the combination $\sigma_8(\Omega_{\rm m}/0.27)^\alpha$, which is the direction orthogonal to the $\Omega_{\rm m}-\sigma_8$ degeneracy 'banana'. To obtain α, we fit a power law to the log-posterior values using histograms with optimal bin numbers for estimating the posterior density (Scott 1979) (Fig. 10). We also discuss constraints on Ω_Λ (for cases with free curvature) and w_0 (for wCDM models). Table 3 shows the combined constraints from CFHTLenS+*WMAP*7 and CFHTLenS+*WMAP*7+BOSS+R09. The comparison between cosmological models is shown in Table 4 and described in Section 5.4.

5.1 $\Omega_{\rm m}$ and σ_8

5.1.1 Flat ΛCDM

For a flat ΛCDM universe, the constraints in the $\Omega_{\rm m} - \sigma_8$ plane (left panel of Fig. 10) from CFHTLenS are nearly orthogonal to the ones for *WMAP*7. CFHTLenS improves the joint constraints for these parameters by a factor of 2. Lensing plus CMB constrains $\Omega_{\rm m}$ and σ_8 to better than 5 per cent and 2 per cent, respectively. Adding BOSS and R09 decreases the error on $\Omega_{\rm m}$ to 3.5 per cent, but does not improve the constraint on σ_8.

5.1.2 Flat wCDM

If the dark-energy equation-of-state parameter w_0 is kept free, CMB and lensing display the same degeneracy direction between $\Omega_{\rm m}$ and σ_8 (left-hand panel of Fig. 11). Combining both probes only partially lifts this degeneracy; the uncertainty on $\Omega_{\rm m}$ remains at the 25 per cent level. This uncertainty decreases to 10 per cent with the addition of the BOSS BAO distance measure.

The value of the Hubble constant from both CFHTLenS+*WMAP*7 ($h = 0.66^{+0.11}_{-0.07}$) and BOSS+*WMAP*7 ($h = 0.65^{+0.08}_{-0.04}$) is slightly lower when compared to the R09 result, $h = 0.742 \pm 0.036$, although it is within the 1σ error bar. Since h is degenerate with all other parameters except $n_{\rm s}$, those parameter means change with the inclusion of the R09 prior. This causes the relatively large $\Omega_{\rm m}$ and $\Omega_{\rm b}$ and low σ_8 if R09 is not added. The joint Hubble constant with all four probes is $h = 0.691^{+0.032}_{-0.029}$.

[14] http://www.lanl.gov/projects/cosmology/CosmicEmu
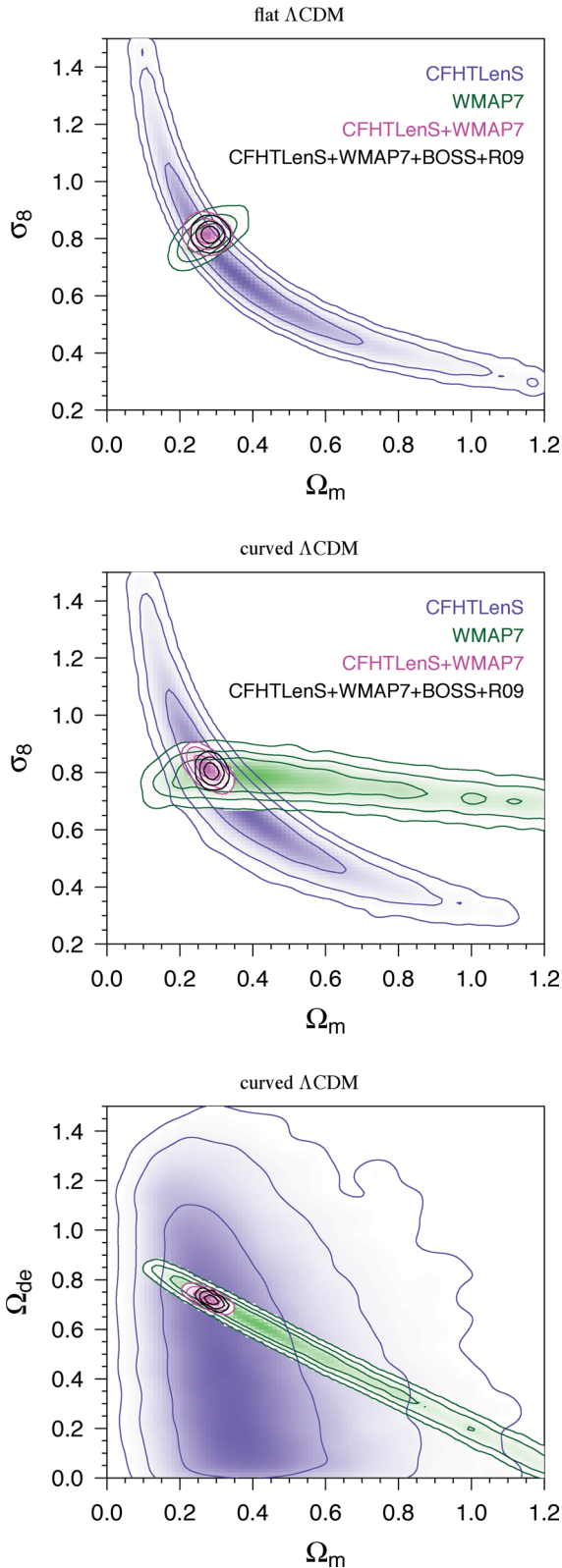
Figure 10. Marginalized posterior density contours (68.3 per cent, 95.5 per cent, 99.7 per cent) for CFHTLenS (blue contours), *WMAP*7 (green), CFHTLenS+*WMAP*7 (red) and CFHTLenS+*WMAP*7+BOSS+R09 (black). The model is flat ΛCDM (left-hand panel) and curved ΛCDM (middle and right panels), respectively.

5.1.3 Curved ΛCDM

With curvature left free and no additional priors, CMB anisotropies cannot determine Ω_m anymore, since there is a degeneracy between matter density, curvature and the Hubble constant. Lensing, however, shows a similar dependency on Ω_m and σ_8 to the flat model case. Therefore, the improvement on Ω_m from CFHTLenS + *WMAP*7 with respect to *WMAP*7 alone is an order of magnitude, to yield an 8 per cent error. The joint error on σ_8 is 3.5 per cent.

5.1.4 Curved wCDM

The Ω_m–σ_8 degeneracy holds nearly the same as in the previous cases of models with fewer parameters, as displayed in the left-hand panel of Fig. 12. The value of $\sigma_8(\Omega_m/0.25)^\alpha$ is slightly increased but well within the error bars. The joint CFHTLenS+*WMAP*7 results on Ω_m and σ_8 are similar to the flat wCDM case.

The BOSS+R09+*WMAP*7 results indicate a slightly smaller Ω_m and larger σ_8. The joint CFHTLenS+*WMAP*7+BOSS+R09 allowed region is therefore on the upper end of the CFHTLenS+*WMAP*7 banana. The reason for this is, as in the flat wCDM case, the degeneracy of Ω_m and σ_8 with the Hubble constant. *WMAP*7 alone prefers a low value, $h = 0.5^{+0.14}_{-0.13}$, which increases to $h = 0.73 \pm 0.04$ when BOSS+R09 is added. As a consequence, Ω_m decreases and σ_8 increases. On the other hand, adding CFHTLenS to *WMAP*7 leaves the Hubble constant at the relatively low value of $h = 0.60^{+0.08}_{-0.06}$.

5.2 Dark energy

For the following results on the dark-energy equation-of-state parameter w, we use the flat prior $[-3.5; 0.5]$.

5.2.1 Flat wCDM

2D weak gravitational lensing alone is not able to tightly constrain dark energy, in contrast with 3D tomographic weak lensing. The 68 per cent confidence limits for w_0 (flat wCDM) are of the order of unity, $w_0 = -1.2^{+0.8}_{-1.4}$. In combination with *WMAP*7 only, these errors decrease by a factor of 4, and w_0 gets constrained to about 30 per cent. The CFHTLenS+*WMAP*7+BOSS constraints on dark energy are $w_0 = -0.78^{+0.09}_{-0.11}$. We discuss this deviation from ΛCDM in Section 7. Adding the R09 prior on H_0 does not reduce the error but shifts the mean to the ΛCDM value, $w_0 = -0.99^{+0.11}_{-0.12}$.

5.2.2 Curved wCDM

The case of dark energy is similar in the curved case. CFHTLenS alone results in $w_0 = -1.2^{+0.9}_{-1.8}$. Adding *WMAP*7 reduced this uncertainty to 30 per cent. CFHTLenS+*WMAP*7+BOSS yield $w_0 = -0.81^{+0.14}_{-0.19}$. Adding the R09 prior on H_0, we find the ΛCDM-consistent value of $w_0 = -1.10^{+0.15}_{-0.16}$.

5.3 Curvature

CFHTLenS helps to improve the constraint on the curvature density Ω_K. For ΛCDM, the uncertainty decreases by a factor of 10 from around 0.1 (*WMAP*7 alone) to 0.01 (CFHTLenS+*WMAP*7). Adding BOSS+R09 decreases the error by another factor of 2 to around 0.005. The combined constraints are thus consistent with a flat universe within 5×10^{-3}. For a wCDM model, this uncertainty is of the same order.

Table 3. Cosmological parameter results with 68 per cent confidence intervals. The first line for each parameter shows CFHTLenS+*WMAP*7, and the second line is CFHTLenS+*WMAP*7+BOSS+R09. Asterisks (*) indicate a deduced parameter. The four columns correspond to the four different models.

Parameter	Flat ΛCDM	Flat wCDM	Curved ΛCDM	Curved wCDM
Ω_m	$0.274^{+0.013}_{-0.012}$	$0.325^{+0.082}_{-0.076}$	$0.275^{+0.023}_{-0.021}$	$0.377^{+0.098}_{-0.079}$
	$0.283^{+0.010}_{-0.009}$	$0.287^{+0.026}_{-0.023}$	$0.286^{+0.011}_{-0.010}$	$0.271^{+0.028}_{-0.025}$
σ_8*	$0.815^{+0.016}_{-0.014}$	$0.77^{+0.11}_{-0.07}$	$0.815^{+0.030}_{-0.025}$	$0.715^{+0.090}_{-0.070}$
	$0.814^{+0.015}_{-0.014}$	$0.809^{+0.039}_{-0.035}$	0.804 ± 0.018	$0.826^{+0.037}_{-0.039}$
w_0		$-0.86^{+0.22}_{-0.32}$		$-0.72^{+0.20}_{-0.24}$
	-1	$-0.99^{+0.11}_{-0.12}$	-1	$-1.10^{+0.15}_{-0.16}$
Ω_de			$0.726^{+0.016}_{-0.015}$	$0.628^{+0.074}_{-0.094}$
	$1-\Omega_\mathrm{m}$	$1-\Omega_\mathrm{m}$	$0.7186^{+0.099}_{-0.014}$	$0.735^{+0.028}_{-0.032}$
Ω_K*			-0.0003 ± 0.0086	$-0.005^{+0.011}_{-0.012}$
	0	0	$-0.0047^{+0.0045}_{-0.0047}$	$-0.0063^{+0.0064}_{-0.0045}$
h	$0.702^{+0.014}_{-0.013}$	$0.66^{+0.11}_{-0.07}$	$0.703^{+0.037}_{-0.033}$	$0.605^{+0.082}_{-0.062}$
	0.693 ± 0.010	$0.691^{+0.032}_{-0.029}$	0.683 ± 0.014	$0.702^{+0.032}_{-0.030}$
Ω_b	0.0456 ± 0.0012	$0.054^{+0.014}_{-0.013}$	$0.0457^{+0.0045}_{-0.0041}$	$0.064^{+0.018}_{-0.014}$
	0.0465 ± 0.0010	$0.0471^{+0.0046}_{-0.0042}$	$0.0482^{+0.0020}_{-0.0019}$	$0.0457^{+0.0047}_{-0.0042}$
n_S	0.966 ± 0.013	0.966 ± 0.014	$0.965^{+0.013}_{-0.014}$	$0.970^{+0.014}_{-0.013}$
	0.961 ± 0.012	$0.959^{+0.013}_{-0.014}$	0.966 ± 0.013	$0.964^{+0.013}_{-0.014}$
τ	$0.089^{+0.016}_{-0.014}$	$0.088^{+0.016}_{-0.014}$	$0.088^{+0.016}_{-0.014}$	$0.088^{+0.017}_{-0.013}$
	$0.083^{+0.014}_{-0.013}$	$0.084^{+0.015}_{-0.013}$	$0.088^{+0.016}_{-0.014}$	$0.087^{+0.015}_{-0.014}$
$10^9 \Delta_R^2$	$2.441^{+0.090}_{-0.084}$	$2.433^{+0.095}_{-0.087}$	$2.445^{+0.095}_{-0.090}$	$2.395^{+0.093}_{-0.095}$
	$2.457^{+0.088}_{-0.081}$	$2.465^{+0.097}_{-0.089}$	$2.422^{+0.095}_{-0.088}$	$2.425^{+0.094}_{-0.089}$

Table 4. Bayesian evidence E and Bayes' factor with respect to ΛCDM for four different cosmological models. The columns for w_0 and Ω_K show the prior range for those two parameters. The data are CFHTLenS+*WMAP*7 (fourth column) and CFHTLenS+*WMAP*7+BOSS+R09 (last column), respectively.

Name	w_0	Ω_K	$\ln B_{01}$ CFHTLenS+*WMAP*7	$\ln B_{01}$ CFHTLenS+*WMAP*7 +BOSS+R09
ΛCDM	-1	0	0	0
Curved ΛCDM	-1	$[0; 2]$	-3.84	-4.0
Flat wCDM	$[-1; -1/3]$	0	0.42	0.58
Curved wCDM	$[-1; -1/3]$	$[0; 2]$	-3.19	-4.8

5.4 Model comparison

In Table 4, the evidence E and the logarithms of the evidence ratios, $\ln B_{01} = \ln E_0/E_1$, between the baseline flat Λ model and the other three models are shown. Here, E_0 is the evidence for flat ΛCDM and E_1 the evidence for one of the three models curved ΛCDM, flat wCDM and curved wCDM, respectively. B_{01} is called the Bayes factor between model '0' and model '1'.

An empirical scale to interpret such evidence values was suggested by Jeffreys (1961) (see also Trotta 2008). Accordingly, two models are not distinguishable when $|\ln B_{01}| < 1$. If the log-Bayes factor is between 1 and 2.5, the evidence is called weak. Moderate evidence is assumed for $2.5 < |\ln B_{01}| < 5$, and strong for values larger than that.

We compute the evidence for the two cases of probes CFHTLenS+*WMAP*7 and CFHTLenS+*WMAP*7+BOSS+R09. Although the evidence for the flat dark-energy model is slightly larger than the one for the cosmological constant model, the models are indistinguishable: their respective evidence values, or posterior odds, are within a factor of 2. The evidence against curved models is moderate, with log-Bayes factor ratios between 3.2 and 4.8, or posterior odd ratios between 25 and 130 in favour of flat ΛCDM. The significance increases when adding BOSS and R09, but stays in the moderate range. We remind the reader that the dark-energy models considered here have the flat prior $[-1; -1/3]$ for w, which corresponds to an accelerating non-phantom dark-energy component.

6 COMPARISON OF WEAK-LENSING STATISTICS, SYSTEMATICS AND CONSISTENCY TESTS

In this section we obtain cosmological constraints from the derived second-order estimators which were discussed in Section 2.2. The
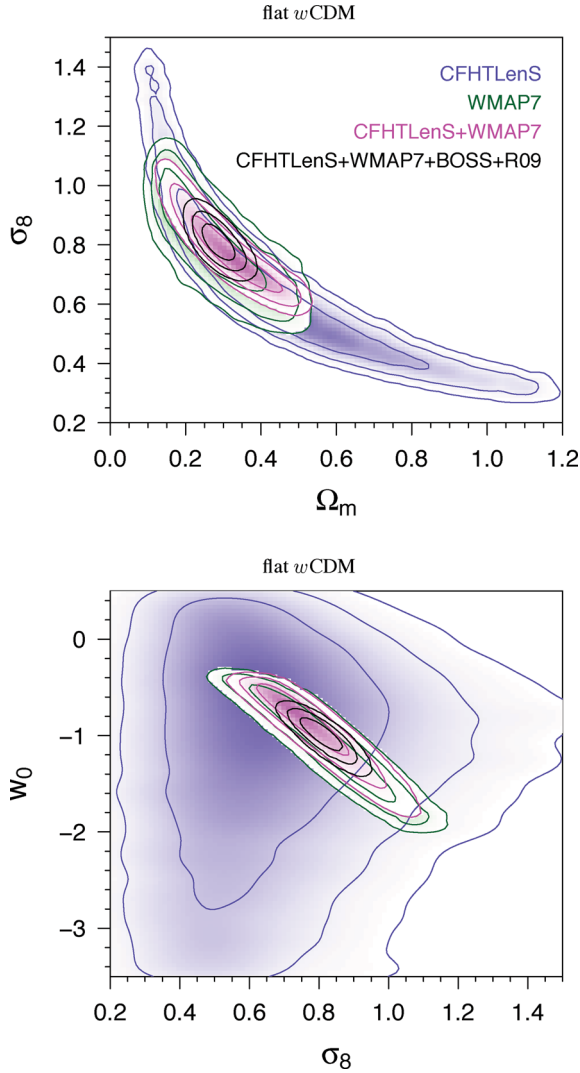
Figure 11. Marginalized posterior density contours (68.3 per cent, 95.5 per cent, 99.7 per cent) for CFHTLenS (blue contours), *WMAP*7 (green), CFHTLenS+*WMAP*7 (magenta) and CFHTLenS+*WMAP*7+BOSS+R09 (black). The model is flat wCDM.
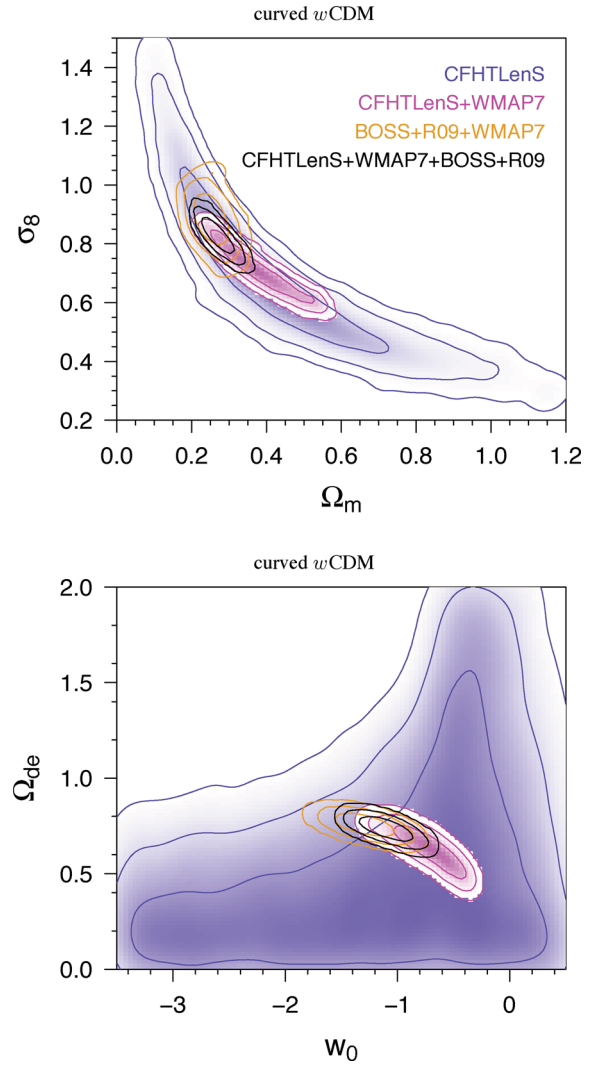

Figure 12. Marginalized posterior density contours (68.3 per cent, 95.5 per cent, 99.7 per cent) for CFHTLenS (blue contours), *WMAP*7 (green), CFHTLenS+*WMAP*7 (magenta) and CFHTLenS+*WMAP*7+BOSS+R09 (black). The model is curved wCDM.

following tests are all performed under a flat ΛCDM model. The results are listed in Table 5.

6.1 Derived second-order functions

As expected, the constraints from the derived second-order estimators are less tight than from the 2PCFs, since they always involve information loss. Moreover, we use a smaller range of angular scales, cutting off both on the lower and higher end, as discussed before. All estimators give consistent results.

Aperture-mass dispersion and top-hat shear rms give very similar constraints compared to the 2PCFs. The position and slope of the banana are nearly identical, although the width is larger by a factor of 2 (see Table 2). For $\langle |\gamma|^2 \rangle$, we analyse two approaches of dealing with the finite survey–size E-/B-mode leakage:

(i) *Ignoring the leakage.* We fit theoretical models of the top-hat shear rms (equations 7, A3) directly to the measured E-mode data points $\langle |\gamma|^2 \rangle(\theta_i)$. Since power is lost due to the leakage, we expect $\sigma_8 \Omega_{\mathrm{m}}^\alpha$ to be biased low.

Table 5. Constraints from CFHTLenS orthogonal to the Ω_{m}–σ_8 degeneracy direction. The main results from the 2PCF (first row) are compared to other estimators.

Data	α	$\sigma_8 \, (\Omega_{\mathrm{m}}/0.27)^\alpha$
2PCF	0.59 ± 0.02	0.79 ± 0.03
$\langle M_{\mathrm{ap}}^2 \rangle$	0.70 ± 0.02	0.79 ± 0.06
$\langle |\gamma|^2 \rangle$ (ignoring offset)	0.60 ± 0.03	$0.78^{+0.04}_{-0.05}$
$\langle |\gamma|^2 \rangle$ (constant offset)	0.58 ± 0.03	$0.80^{+0.03}_{-0.04}$
$\mathcal{R}_E$	0.56 ± 0.02	$0.80^{+0.03}_{-0.04}$
COSEBIs ($\vartheta_{\mathrm{max}} = 100$ arcmin)	0.60 ± 0.02	$0.79^{+0.04}_{-0.06}$
COSEBIs ($\vartheta_{\mathrm{max}} = 250$ arcmin)	0.64 ± 0.03	$0.77^{+0.04}_{-0.05}$
2PCF, constant covariance	0.60 ± 0.03	$0.78^{+0.03}_{-0.04}$
2PCF ($\vartheta \geq 17$ arcmin)	0.65 ± 0.02	0.78 ± 0.04
2PCF ($\vartheta \geq 53$ arcmin)	0.65 ± 0.03	$0.79^{+0.07}_{-0.06}$

(ii) *We add a constant offset of 5.3×10^{-7} to the measured E-mode points.* This corresponds to the theoretical leakage for the *WMAP*7 best-fitting ΛCDM model with $\sigma_8 = 0.8$. On scales $\theta <$ 5 arcmin, the assumption of a constant offset is clearly wrong; however, the constant is two orders of magnitudes smaller than the measured signal and does not influence the result much.

The difference between both cases is about half of the statistical uncertainty (Table 2). More sophisticated ways to deal with this leakage, e.g. going beyond a constant offset, or marginalizing over a parametrized offset, are expected to yield similar results. Since they all have the disadvantage of depending on prior information about a theoretical model which might bias the result towards that model, we do not consider this second-order estimator further.

The function $\mathcal{R}_E$ on scales between $\vartheta_{\max} = 7.5$ and 140 arcmin, for $\eta = \vartheta_{\min}/\vartheta_{\max} = 1/50$ (implying $\vartheta_{\min} = 9$ arcsec, ..., 2.8 arcmin) yields consistent results to the 2PCFs. The results for COSEBIs are consistent with the 2PCFs for both cases of $\vartheta_{\max}$. For $\vartheta_{\max} = 250$ arcmin we find that the modes which are consistent with zero do contain information about cosmology. When only using the first two modes, we obtain $\sigma_8(\Omega_{\rm m}/0.27)^{0.7} = 0.78^{+0.06}_{-0.07}$, corresponding to a larger uncertainty of 30 per cent.

6.2 Robustness and consistency tests

In this section, we test the robustness of our results, by considering various potential systematic effects, and by varying the angular scales and estimators.

6.2.1 Shear calibration covariance

We add the shear calibration $\mathbf{C}_m$ (Section 3.4) covariance to the total shear covariance. The correlation coefficient of $\mathbf{C}_m$ between angular bins is nearly unity, implying that the shear calibration varies very little with angular separation. Since the magnitude of the covariance is much smaller than the statistical uncertainties, the cosmological results are virtually unchanged.

6.2.2 Large scales only

The largest S/N for cosmic shear is on small, non-linear scales. Unfortunately, those scales are the most difficult to model, because of uncertainties in the dark-matter clustering, and baryonic effects on the total power spectrum. To obtain more robust cosmological constraints, we exclude small scales from the 2PCFs in two cases, as follows. First, we use the cut-off $\vartheta_{\rm c} = 17$ arcmin. At this scale, the non-linear halofit prediction of ξ_+ is within 5 per cent of the linear model. Baryonic effects, following Semboloni et al. (2011), are reduced to sub per cent level. The component ξ_-, being more sensitive to small scales, is still highly non-linear at this scale. However, since most of the constraining power is contained in ξ_+, the resulting cosmological constraints will not be very sensitive to non-linearities. Nevertheless, we use a second, more conservative, cut-off of $\vartheta_{\rm c} = 53$ arcmin, where the non-linear models of ξ_- is within a factor of 2 of the linear one. On these scales, ξ_- is affected by baryonic physics by less than 5 per cent (Semboloni et al. 2011). In both cases, we obtain a mean parameter value for $\sigma_8(\Omega_{\rm m}/0.27)^{0.7}$ which is consistent with the result from all angular scales down to an arcmin. In comparison, the error bars on this combined parameter are larger by 30 per cent for $\vartheta_{\rm c} = 17$ arcmin, and 100 per cent for $\vartheta_{\rm c} = 53$ arcmin (see Table 2).

6.2.3 Reduced shear

Since the weak-lensing observable is not the shear γ, but the reduced shear $g = \gamma/(1 - \kappa)$, the relation between the shear correlation function and the convergence power spectrum ignores higher-order terms (see for an overview, Krause & Hirata 2010). The full calculation of only the third-order terms, involving the convergence bispectrum, is very time-consuming and unfeasible for Monte Carlo sampling, requiring the calculation of tens of thousands of different models.

Instead, we explore the fitting formulae from Kilbinger (2010) as a good approximation of reduced-shear effects. For a *WMAP*7 ΛCDM cosmology, the ratio between the 2PCFs with and without taking into account reduced shear is 1 per cent for ξ_+ and 4 per cent for ξ_- at the smallest scale considered, $\vartheta = 0.8$ arcmin. Since the fitting formulae are valid within a small range around the *WMAP*7 cosmology, we use them for the combined Lensing+CMB parameter constraints. The changes in $\Omega_{\rm m}$ and σ_8 for a ΛCDM model are less than a per cent.

6.2.4 Number of simulated lines of sight

Following Huff et al. (2011), we examine the influence of the number of simulated lines of sight on the parameter constraints. We calculate the covariance of $\langle M_{\rm ap}^2 \rangle$ from 110 instead of 184 lines of sight (Section 3.3.4). Using the corresponding Anderson–Hartlap factor α, we find identical results as before and conclude that the number of simulations is easily sufficient for this work.

6.2.5 Non-Gaussian covariance fitting formulae

We replace the non-Gaussian covariance of ξ_+ calculated from the Clone with the fitting formulae from S07 and Sato et al. (2011, hereafter S11), respectively. These works provide prescriptions of the non-Gaussian covariance by rescaling the Gaussian cosmic-variance term by fitting to *N*-body simulations. Since no recipe for ξ_- is given, we use the Gaussian covariance for ξ_- and for the cross-covariance between ξ_+ and ξ_-. We find for $\sigma_8(\Omega_{\rm m}/0.27)^{\alpha}$ the results $0.79^{+0.03}_{-0.04}$ for the S07 case, and $0.78^{+0.03}_{-0.04}$ for S11, recovering the mean value with slightly larger error bars. This shows that our results are not sensitive to the choice of the non-Gaussian covariance.

6.2.6 Cosmology-independent covariance

We compare the two cases of cosmology-dependent covariance (Section 3.3.2), and a constant covariance, fixed to the fiducial model. Contrary to Jee et al. (2012), we find only small differences in the cosmological results. The main effect is a slight increase in the error bars for the constant covariance (see Table 2). In particular, around the region of the fiducial model, the results are basically the same, and therefore, the joint constraints with other probes are virtually unaffected by the choice of the covariance.

7 DISCUSSION AND CONCLUSION

In this paper we present measurements of various second-order shear correlations from weak gravitational lensing by CFHTLenS. Using a single-redshift bin, $0.2 < z_{\rm p} < 1.3$, we obtain cosmological constraints on the matter density, $\Omega_{\rm m}$, and the power-spectrum amplitude, σ_8. Adding *WMAP*7, BOSS and R09 data, we obtain

parameter constraints for flat and curved ΛCDM and dark-energy models, and calculate the Bayesian evidence to compare the probability for each model given the data.

7.1 Second-order shear functions

Along with the 2PCFs ξ_+ and ξ_-, which are the fundamental shear observables, we consider various derived second-order functions, which are able to separate the shear correlation into its E and B mode. The resulting B mode is consistent with zero on all scales. The excess in the E- and B-mode signal that was seen in the CFHTLS-T0003 data (F08) between 50 and 130 arcmin is no longer present. This excess was most likely due to systematics in the earlier data, and the removal of this feature has to be seen as a success of the CFHTLenS analysis. In particular, hints for deviations from General Relativity using the F08 data (Zhao et al. 2010) are not confirmed with CFHTLenS (Simpson et al. 2013).

7.2 Cosmological parameters

The parameter combination which 2D weak lensing can constrain best is $\sigma_8 \Omega_m^\alpha$ with $\alpha \sim 0.6$. CFHTLenS alone, with the 2PCFs, constrains the combination $\sigma_8 (\Omega_m/0.27)^{0.6}$ to 0.787 ± 0.032. To facilitate a comparison with F08, we write our constraints as $\sigma_8 (\Omega_m/0.25)^\alpha = 0.82 \pm 0.03$ (2PCFs), $0.84^{+0.03}_{-0.04}$ (top-hat shear rms) and 0.83 ± 0.06 (aperture-mass dispersion). The exponent α is around 0.6 in all three cases. F08 obtained results with uncertainties between 0.042 and 0.049, although only smoothed second-order quantities were used. The function closest to the 2PCFs is ξ_E, for which F08 found $\sigma_8 (\Omega_m/0.25)^{0.46} = 0.784 \pm 0.049$, corresponding to an uncertainty of 6.2 per cent, compared to 4 per cent in this work. This increase in precision of 50 per cent is consistent with the naive expectation of CFHTLenS to yield smaller error bars by a factor of the square root of the area between CFHTLenS and T0003, which is $\sqrt{129/57} = 1.4$.

Our uncertainty for the top-hat shear rms is about the same as in F08, whereas the aperture-mass dispersion is slightly more poorly constrained in this work. Tighter constraints of 5.5 per cent were found by F08 from $\langle M_{ap}^2 \rangle$, which was used for their combined CFHTLS-T0003 + *WMAP*3 results. The fact that the increase in precision for those smoothed quantities is smaller than expected is most due to the limited parameter range of F08, who used tight priors on the Hubble parameter, $h \in [0.6; 0.8]$ and fixed Ω_b and n_s. In particular the narrow range of h resulted in tighter constraints on Ω_m and σ_8 in F08.

Schrabback et al. (2010) obtained $\sigma_8 (\Omega_m/0.3)^{0.6} = 0.68 \pm 0.11$ from a 2D weak-lensing analysis of the Cosmological Evolution Survey[15] data. The relatively large error bars are dominated by cosmic variance from the very small survey area of 1.64 deg², despite the great depth of the survey. A 3D lensing analysis with a large number of redshift bins (five narrow bins up to $z = 4$ and one broad bin with mean redshift of 1.5) decreases the error bar by 20 per cent, $\sigma_8 (\Omega_m/0.3)^{0.5} = 0.79 \pm 0.09$. This uncertainty is still larger by a factor of 3 than our CFHTLenS 2D constraints, $\sigma_8 (\Omega_m/0.3)^{0.6} = 0.74 \pm 0.03$.

On 168 deg² of SDSS[16] data in the Stripe 82 equatorial region, out to a median redshift of 0.52, Huff et al. (2011) recently obtained $\sigma_8 (\Omega_m/0.264)^{0.67} = 0.65^{+0.12}_{-0.15}$ using a combination of COSE-BIs with $(\vartheta_{min}, \vartheta_{max}) = (1.3, 97.5)$ arcmin and an additional data point of $\xi_+(38$ arcmin). With CFHTLenS we get $\sigma_8 (\Omega_m/0.264)^{0.6} = 0.80 \pm 0.03$ for the 2PCFs and $0.80^{+0.04}_{-0.06}$ for COSEBIs with $\vartheta_{max} = 100$ arcmin.

Recent results from a 2D analysis of the Deep Lens Survey[17] (DLS) yielded the very tight constraints $\Omega_m = 0.26 \pm 0.05$ and $\sigma_8 = 0.87 \pm 0.07$ (Jee et al. 2012). Compared to CFHTLenS, DLS has a greater depth with mean redshift of 1.1 and 17 galaxies per arcmin², but on the other hand covers with 20 deg² a smaller area. The parameter space sampled by DLS is similar to F08, with a tight prior on the Hubble constant and fixed baryon density Ω_b and spectral index n_s.

For all models of dark energy and curvature considered here, the agreement of σ_8 and Ω_m from CFHTLenS with *WMAP*7 is very good. This remains true when BOSS data on the BAO peak are added. However, we find values of w_0 for CFHTLenS+*WMAP*+BOSS which are significantly smaller than -1, both for flat and for curved wCDM models. The reason for this is the near-degeneracy of the dark-energy parameter with the Hubble constant. The latter takes the rather low value of around 0.65 ± 0.1, which results in a high value of w_0. Adding the R09 result increases h and thus also increases w_0, yielding values which are consistent with ΛCDM.

For the flat ΛCDM model, adding CFHTLenS to *WMAP*7 strongly helps reducing error bars on Ω_m and σ_8. The improvement is larger than in the case where BOSS+R09 is joined with *WMAP*7, in particular for σ_8. The curved ΛCDM case sees a slightly different dependence on Ω_K between *WMAP*7+CFHTLenS and *WMAP*7+BOSS+R09, resulting in tight constraints when all four probes are combined. Both cases are emphasized in Fig. 13. In the wCDM case, both CFHTLenS and BOSS cannot improve significantly the dark-energy constraint with respect to *WMAP*7. Only the addition of R09, thereby lifting the w_0–h degeneracy, decreases the error on the dark-energy parameter.

Our results are in very good agreement with the measurement presented in Hudson & Turnbull (2012), who find $\Omega_m = 0.259 \pm 0.045$ and $\sigma_8 = 0.748 \pm 0.035$ for a flat ΛCDM model. This method uses low- and high-z peculiar velocity data only and is therefore complementary and independent of our results.

Recent constraints by Mantz et al. (2010) from the X-ray Röntgensatellit (ROSAT) All-Sky Survey using the cluster mass function for a flat wCDM universe are $\Omega_m = 0.23 \pm 0.04$, $\sigma_8 = 0.82 \pm 0.05$ and $w_0 = -1.01 \pm 0.20$, in agreement with the results presented here. Their relatively low Ω_m is consistent with our result of $\Omega_m = 0.29 \pm 0.02$. When adding CMB (*WMAP*5), SNIa, BAO and the cluster gas fraction to the cluster mass function, Mantz et al. (2010) get $\Omega_m = 0.27 \pm 0.02$. From the optical SDSS maxBCG cluster catalogue, Rozo et al. (2010) obtain for a flat ΛCDM model $\sigma_8 (\Omega_m/0.25)^{0.41} = 0.83 \pm 0.03$. In combination with *WMAP*5, they get $\Omega_m = 0.265 \pm 0.016$ and $\sigma_8 = 0.807 \pm 0.020$, which is again consistent with this work.

7.3 Model comparison

Using the Bayesian evidence, we computed the posterior odds for various cosmological models. Starting from the basic ΛCDM model, we tested extensions of this model which included curvature Ω_K and the dark-energy equation-of-state parameter w. We find no evidence against the standard flat ΛCDM model.

---

[15] http://cosmos.astro.caltech.edu
[16] Sloan Digital Sky Survey; www.sdss.org

[17] http://dls.physics.ucdavis.edu
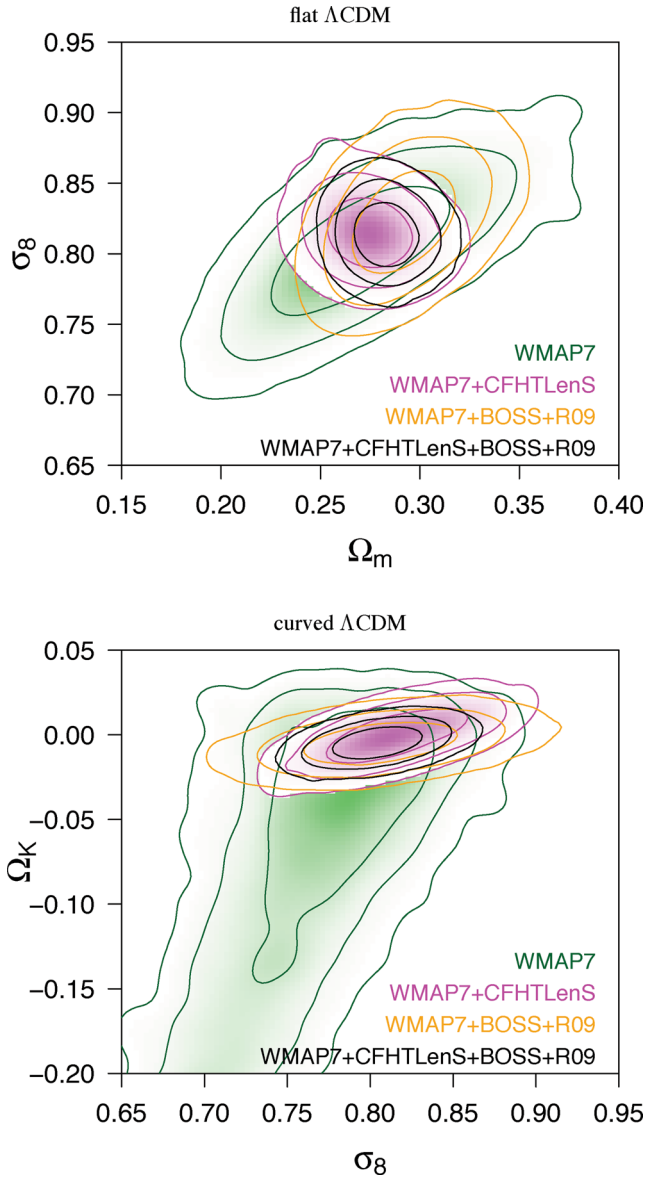
Figure 13. Marginalized posterior density contours (68.3 per cent, 95.5 per cent, 99.7 per cent) for *WMAP*7 (green), *WMAP*7+CFHTLenS (magenta), *WMAP*7+BOSS+R09 (orange) and *WMAP*7+CFHTLenS+BOSS+R09 (black). The model is flat ΛCDM (upper panel) and curved ΛCDM (lower panel), respectively.

The constraints for the larger models with free curvature are consistent with $\Omega_K = 0$. It is therefore not surprising that those more general models are not favoured over models with fixed flat geometry. The larger parameter space from the additional degree of freedom implies a lower predictive capability of those extended models. A good model should not only predict (a priori) the correct parameter range where the result is to be found (a posteriori), but also make a specific and accurate prediction; in other words, it should have a narrow prior range compared to the posterior. A lack of predictive capability is penalized by the Bayesian evidence.

In contrast to the two non-flat models (curved ΛCDM and curved wCDM), the flat wCDM universe is indistinguishable from a flat model with cosmological constant. This can be understood by looking at the respective additional parameter constraints beyond ΛCDM, that is, Ω_{de} for the curved and w_0 for wCDM. Compared to

the corresponding prior, the allowed posterior range for Ω_{de} is a lot smaller than the one for w_0 since the latter parameter is less tightly constrained. Therefore, the curved models are less predictive, corresponding to a lower evidence. Both the very tight constraints on Ω_K, with error of about 0.005, and the moderate Bayesian evidence in favour of a flat model strengthen the emerging picture that we live indeed in a Universe with zero curvature.

of this paper (MK, LF, CH and FS) followed by two alphabetical groups. The first group includes key contributers to the science analysis and interpretation in this paper, the founding core team and those whose long-term significant effort produced the final CFHTLenS data product. The second group covers members of the CFHTLenS team who made a significant contribution to either the project, this paper or both, and external authors. JHD, SV and LVW produced the numerical simulations and, with CH, created the clone. The CFHTLenS collaboration was co-led by CH and LVW, and the CFHTLenS Cosmology Working Group was led by TDK.

REFERENCES

Albrecht A. et al., 2006, preprint (arXiv:0609591)

Anderson T. W., 2003, An Introduction to Multivariate Statistical Analysis, 3rd edn. Wiley-Interscience

Anderson L. et al., 2012, MNRAS, 427, 3435

Asgari M., Schneider P., Simon P., 2012, A&A, 542, A122

Bartelmann M., 2010, Classical Quantum Gravity, 27, 233001

Bartelmann M., Schneider P., 2001, Phys. Rep., 340, 297

Becker M. R., 2012, preprint (arXiv:1208.0068)

Benítez N., 2000, ApJ, 536, 571

Benjamin J. et al., 2007, MNRAS, 381, 702

Benjamin J., Van Waerbeke L., Ménard B., Kilbinger M., 2010, MNRAS, 408, 1168

Benjamin J. et al., 2013, MNRAS, submitted (arXiv:1212.3327)

Cappé O., Guillin A., Marin J.-M., Robert C., 2004, J. Comput. Graph. Stat., 13, 907

Cappé O., Douc R., Guillin A., Marin J.-M., Robert C., 2008, Stat. Comput., 18, 447

Conley A. et al., 2011, ApJS, 192, 1

Coupon J. et al., 2009, A&A, 500, 981

Crittenden R. G., Natarajan P., Pen U.-L., Theuns T., 2002, ApJ, 568, 20

Doré O. et al., 2008, Phys. Rev. D, accepted (arXiv:0712.1599)

Dunkley J. et al., 2009, ApJS, 180, 306

Eifler T., 2011, MNRAS, 1490

Eifler T., Kilbinger M., Schneider P., 2008, A&A, 482, 9

Eifler T., Schneider P., Hartlap J., 2009, A&A, 502, 721

Erben T. et al., 2009, A&A, 493, 1197

Erben T. et al., 2013, MNRAS, submitted (arXiv:1210.8156)

Fu L., Kilbinger M., 2010, MNRAS, 401, 1264

Fu L. et al., 2008, A&A, 479, 9 (F08)

Giannantonio T., Porciani C., Carron J., Amara A., Pillepich A., 2012, MNRAS, 422, 2854

Harnois-Déraps J., Vafaei S., Van Waerbeke L., 2012, MNRAS, 426, 1262

Hartlap J., Simon P., Schneider P., 2007, A&A, 464, 399

Hartlap J., Schrabback T., Simon P., Schneider P., 2009, A&A, 504, 689

Hartlap J., Hilbert S., Schneider P., Hildebrandt H., 2011, A&A, 528, A51

Heitmann K., Higdon D., White M., Habib S., Williams B. J., Lawrence E., Wagner C., 2009, ApJ, 705, 156

Heitmann K., White M., Wagner C., Habib S., Higdon D., 2010, ApJ, 715, 104

Heymans C. et al., 2012, MNRAS, 427, 146

Hilbert S., Hartlap J., Schneider P., 2011, A&A, 536, A85

Hildebrandt H. et al., 2012, MNRAS, 421, 2355

Hirata C. M., Seljak U., 2004, Phys. Rev. D, 70, 063526

Hoekstra H., Jain B., 2008, Annu. Rev. Nucl. Part. Sci., 58, 99

Hoekstra H. et al., 2006, ApJ, 647, 116

Hu W., 1999, ApJ, 522, L21

Hudson M. J., Turnbull S. J., 2012, ApJ, 751, L30

Huff E. M., Eifler T., Hirata C. M., Mandelbaum R., Schlegel D., Seljak U., 2011, preprint (arXiv:1112.3143)

Ilbert O. et al., 2006, A&A, 457, 841

Jee M. J., Tyson J. A., Schneider M. D., Wittman D., Schmidt S., Hilbert S., 2012, ApJ, accepted (arXiv:1210.2732)

Jeffreys H., 1961, Theory of Probability, 3rd edn., Oxford Classic Texts in the Physical Sciences. Oxford University Press, Oxford

Jing Y. P., Zhang P., Lin W. P., Gao L., Springel V., 2006, ApJ, 640, L119

Joachimi B., Mandelbaum R., Abdalla F. B., Bridle S. L., 2011, A&A, 527, A26

Kaiser N., 1992, ApJ, 388, 272

Kayo I., Takada M., Jain B., 2013, MNRAS, 429, 344

Keitel D., Schneider P., 2011, A&A, 534, A76

Kilbinger M., 2010, A&A, 519, A19

Kilbinger M., Schneider P., 2004, A&A, 413, 465

Kilbinger M., Schneider P., Eifler T., 2006, A&A, 457, 15

Kilbinger M. et al., 2009, A&A, 497, 677

Kilbinger M. et al., 2010, MNRAS, 405, 2381

Kilbinger M., Benabed K., Cappe O., Cardoso J.-F., Fort G., Prunet S., Robert C. P., Wraith D., 2011, preprint (arXiv:1101.0950)

Kirk D., Bridle S., Schneider M., 2010, MNRAS, 408, 1502

Komatsu E. et al., 2011, ApJS, 192, 18

Krause E., Hirata C. M., 2010, A&A, 523, A28

Larson D. et al., 2011, ApJS, 192, 16

Laureijs R. et al., 2011, preprint (arXiv:1110.3193)

Lawrence E., Heitmann K., White M., Higdon D., Wagner C., Habib S., Williams B., 2010, ApJ, 713, 1322

Lewis A., Challinor A., Lasenby A., 2000, ApJ, 538, 473

McDonald P., Trac H., Contaldi C., 2006, MNRAS, 366, 547

Mandelbaum R. et al., 2011, MNRAS, 410, 844

Mantz A., Allen S. W., Rapetti D., Ebeling H., 2010, MNRAS, 406, 1759

Miller L. et al., 2013, MNRAS, in press (arXiv:1210.8201)

Munshi D., Valageas P., Van Waerbeke L., Heavens A., 2008, Phys. Rep., 462, 67

Pen U.-L., Van Waerbeke L., Mellier Y., 2002, ApJ, 567, 31

Pires S., Starck J.-L., Amara A., Réfrégier A., Teyssier R., 2009, A&A, 505, 969

Power C., Knebe A., 2006, MNRAS, 370, 691

Refregier A., Amara A., Kitching T., Rassat A., 2011, A&A, 528, A33

Riess A. G. et al., 2009, ApJ, 699, 539 (R09)

Rozo E. et al., 2010, ApJ, 708, 645

Rudd D. H., Zentner A. R., Kravtsov A. V., 2008, ApJ, 672, 19

Sánchez A. G. et al., 2012, MNRAS, 425, 415

Sato M., Hamana T., Takahashi R., Takada M., Yoshida N., Matsubara T., Sugiyama N., 2009, ApJ, 701, 945

Sato M., Ichiki K., Takeuchi T. T., 2010, Phys. Rev. Lett., 105, 251301

Sato M., Takada M., Hamana T., Matsubara T., 2011, ApJ, 734, 76 (S11)

Schneider P., Kilbinger M., 2007, A&A, 462, 841

Schneider P., Van Waerbeke L., Jain B., Kruse G., 1998, MNRAS, 296, 873

Schneider P., Van Waerbeke L., Mellier Y., 2002a, A&A, 389, 729

Schneider P., Van Waerbeke L., Kilbinger M., Mellier Y., 2002b, A&A, 396, 1

Schneider P., Eifler T., Krause E., 2010, A&A, 520, A116

Schrabback T. et al., 2010, A&A, 516, A63

Scott D., 1979, Biometrika, 66, 605

Semboloni E. et al., 2005, A&A, 452, 51

Semboloni E., Van Waerbeke L., Heymans C., Hamana T., Colombi S., White M., Mellier Y., 2007, MNRAS, 375, L6 (S07)

Semboloni E., Hoekstra H., Schaye J., van Daalen M. P., McCarthy I. G., 2011, MNRAS, 417, 2020

Simpson F. et al., 2013, MNRAS, in press (arXiv:1212.3339)

Smith R. E. et al., 2003, MNRAS, 341, 1311

Suzuki N. et al., 2012, ApJ, 746, 85

Takada M., Jain B., 2009, MNRAS, 395, 2065

Tereno I., Schimd C., Uzan J.-P., Kilbinger M., Vincent F., Fu L., 2009, A&A, 712, 657

Trotta R., 2008, Contemporary Phys., 49, 71

Uzan J.-P., 2010, General Relativ. Gravitation, 42, 2219

Vafaei S., Lu T., van Waerbeke L., Semboloni E., Heymans C., Pen U.-L., 2010, Astropart. Phys., 32, 340

Vallinotto A., Dodelson S., Schimd C., Uzan J.-P., 2007, Phys. Rev. D, 75, 103509

Van Waerbeke L., Mellier Y., 2003, preprint (astro-ph/0305089)

Vanderveld R. A., Mortonson M. J., Hu W., Eifler T., 2012, Phys. Rev. D, 85, 103518

Wraith D., Kilbinger M., Benabed K., Cappé O., Cardoso J.-F., Fort G., Prunet S., Robert C. P., 2009, Phys. Rev. D, 80, 023507

Zhao G., Giannantonio T., Pogosian L., Silvestri A., Bacon D. J., Koyama K., Nichol R. C., Song Y., 2010, Phys. Rev. D, 81, 103510

APPENDIX A: FILTER FUNCTIONS

We give expressions of the filter functions F_+, F_-, needed to calculate the derived second-order shear observables from the shear correlation functions (equation 6). See Table 1 for the relation between $F_{\pm}$ and the following functions and the integration ranges.

A1 Aperture-mass dispersion

The filter functions for the aperture-mass dispersion, defined in Schneider et al. (2002a), are for $x < 2$

$$T_+(x) = \frac{6(2 - 15x^2)}{5}\left[1 - \frac{2}{\pi}\arcsin(x/2)\right] + \frac{x\sqrt{4 - x^2}}{100\pi}$$
$$\times \left(120 + 2320x^2 - 754x^4 + 132x^6 - 9x^8\right);$$

$$T_-(x) = \frac{192}{35\pi}x^3\left(1 - \frac{x^2}{4}\right)^{7/2}. \tag{A1}$$

The functions have finite support, and are set to zero for $x > 2$. The Fourier-space filter function for the aperture-mass dispersion (equation 7) is

$$\hat{U}(\ell) = \hat{U}_\theta(\ell) = \frac{24J_4(\theta\ell)}{(\theta\ell)^2}. \tag{A2}$$

A2 Top-hat shear rms

For the top-hat shear rms, the real-space filter functions are

$$S_+(x) = \frac{1}{\pi}\left[4\arccos(x/2) - x\sqrt{4 - x^2}\right]H(2 - x);$$

$$S_-(x) = \frac{1}{\pi x^4}$$
$$\times \left[x\sqrt{4 - x^2}(6 - x^2) - 8(3 - x^2)\arcsin(x/2)\right], \tag{A3}$$

where H is the Heaviside step function. Thus, S_+ has support $[0; 2]$ whereas S_- has infinite support. The Fourier transform of S_+ is

$$\hat{U}(\ell) = \hat{U}_\theta(\ell) = \frac{2J_1(\theta\ell)}{(\theta\ell)^2}. \tag{A4}$$

A3 Optimized ring statistic

To obtain an E-/B-mode decomposition of the 2PCF on a finite angular range $[\vartheta_{min}; \vartheta_{max}]$ via the sum in equation (6), two integral conditions for the filter function F_+ need to be fulfilled (Schneider & Kilbinger 2007):

$$\int_{\vartheta_{min}}^{\vartheta_{max}} d\vartheta\, \vartheta\, F_+(\vartheta) = \int_{\vartheta_{min}}^{\vartheta_{max}} d\vartheta\, \vartheta^3 F_+(\vartheta) = 0. \tag{A5}$$

The function F_- can be obtained by an integral over F_+, which follows from the relation equation (7), see Schneider et al. (2002a). Apart from these conditions, the functions $F_{\pm}$ can be freely chosen.

For the optimized ring statistics, the filter functions corresponding to $\mathcal{R}_{E,B}$ are linear combinations of Chebyshev polynomials of the second kind,

$$T_+(\vartheta) = \tilde{T}_+\left(x = \frac{2\vartheta - \vartheta_{max} - \vartheta_{min}}{\vartheta_{max} - \vartheta_{min}}\right)$$
$$= \sum_{n=0}^{N-1} a_n U_n(x); \tag{A6}$$

$$U_n(x) = \frac{\sin[(n+1)\arccos x]}{\sin(\arccos x)}. \tag{A7}$$

The coefficients a_n can be chosen freely, under the condition that $\mathcal{R}_{E,B}$ are pure E- and B-mode components, respectively. We take the a_n from Fu & Kilbinger (2010), which minimized the Ω_m-σ_8 1σ-area using the CFHTLS-T0003 survey setting, and for fixed $\eta = \vartheta_{min}/\vartheta_{max} = 1/50$. For a fixed η, $\mathcal{R}_{E,B}$ depends on only one angular scale θ, which we take to be ϑ_{max}.

A4 COSEBIs

The COSEBIs filter functions we use here are polynomials in the logarithm of the angular scale θ,

$$T_{+,n}^{\log}(\vartheta) = t_{+,n}^{\log}\left[z = \ln\left(\frac{\vartheta}{\vartheta_{min}}\right)\right]$$
$$= N_n\sum_{j=0}^{n+1} c_{nj}z^j = N_n\prod_{j=1}^{n+1}(z - r_{nj}). \tag{A8}$$

The polynomials $t_{+,n}^{\log}(z)$ have been constructed in Schneider et al. (2010) using equation (A5) as an orthonormal and complete set of functions. The coefficients c_{nj} are fixed by integral conditions that assure the E-/B-mode decomposition of the 2PCF on a finite angular integral. They are given by a linear system of equations, which is given in Schneider et al. (2010). To solve this system, a very high numerical accuracy is needed. We use the MATHEMATICA program given in Schneider et al. (2010) to obtain the coefficients for a given ϑ_{min} and ϑ_{max}, and store the zeros r_{ni}, for which a lower accuracy is sufficient. The function F_- is then calculated using equations (38) and (39) from Schneider et al. (2010).

Both for COSEBIs and for FK10, no closed expressions for the Hankel transforms of $T_{\pm}$ have been found (yet); neither for the Fourier-space counterparts, apart form the linear COSEBIs (Asgari et al. 2012). To obtain the theoretical predictions for these functions, we first calculate $\xi_{\pm}$ via equation (4), and use equation (6) to obtain the COSEBIs prediction.

To calculate the numerical integration over the correlation function (equation 6) with high enough precision, we split up the interval $[0; z_{max}]$ into 10 pieces, and perform a Romberg-integration on each piece with relative precision of 10^{-6}. The resulting numerical B mode is smaller than 10^{-15} for modes $n \le 10$, which is about three orders of magnitudes smaller than the predicted E mode.

APPENDIX B: CFHTLENS SECOND-ORDER WEAK-LENSING DATA

The measured 2PCFs as shown in Fig. 6. We list the data points and the total error in Table B1. The full covariance is available on request or via the web page http://cfhtlens.org. The derived second-order E- and B-mode functions are listed in Tables B2 to B5.

Table B1. The CFHTLenS 2PCFs ξ_+ and ξ_-, for different angular scales ϑ (see Section 3.2). The values of σ indicate the error from the total covariance diagonal (Section 3.3.1). The covariance is the one at the fiducial Clone cosmology.

ϑ (arcmin)	$\xi_+(\vartheta)$	$\sigma[(\xi_+(\vartheta)]$	$\xi_-(\vartheta)$	$\sigma[(\xi_-(\vartheta)]$
0.9	1.411×10^{-4}	2.686×10^{-5}	1.610×10^{-5}	2.621×10^{-5}
1.2	6.619×10^{-5}	1.586×10^{-5}	-1.209×10^{-5}	1.491×10^{-5}
1.6	7.438×10^{-5}	1.223×10^{-5}	-7.580×10^{-6}	1.123×10^{-5}
2.2	4.162×10^{-5}	9.507×10^{-6}	2.600×10^{-5}	8.486×10^{-6}
2.9	5.298×10^{-5}	7.438×10^{-6}	1.067×10^{-5}	6.426×10^{-6}
3.9	2.923×10^{-5}	5.864×10^{-6}	1.738×10^{-5}	4.892×10^{-6}
5.2	2.287×10^{-5}	4.669×10^{-6}	4.607×10^{-6}	3.755×10^{-6}
7.0	1.583×10^{-5}	3.745×10^{-6}	1.306×10^{-5}	2.892×10^{-6}
9.4	1.351×10^{-5}	3.045×10^{-6}	7.760×10^{-6}	2.255×10^{-6}
12.5	8.737×10^{-6}	2.494×10^{-6}	9.643×10^{-6}	1.770×10^{-6}
16.8	7.487×10^{-6}	2.088×10^{-6}	4.652×10^{-6}	1.402×10^{-6}
22.4	5.536×10^{-6}	1.791×10^{-6}	5.241×10^{-6}	1.126×10^{-6}
30.0	4.656×10^{-6}	1.605×10^{-6}	2.959×10^{-6}	8.791×10^{-7}
40.2	2.072×10^{-6}	1.457×10^{-6}	2.901×10^{-6}	7.040×10^{-7}
53.7	2.104×10^{-6}	1.310×10^{-6}	1.332×10^{-6}	6.072×10^{-7}
71.7	9.524×10^{-8}	1.153×10^{-6}	7.075×10^{-7}	5.260×10^{-7}
95.5	2.149×10^{-7}	9.903×10^{-7}	2.048×10^{-6}	4.496×10^{-7}
125.3	2.660×10^{-7}	8.990×10^{-7}	1.240×10^{-6}	4.552×10^{-7}
160.3	5.207×10^{-7}	8.782×10^{-7}	6.247×10^{-7}	4.994×10^{-7}
211.7	4.607×10^{-7}	9.043×10^{-7}	-4.670×10^{-7}	5.690×10^{-7}
296.5	7.331×10^{-8}	9.729×10^{-7}	7.811×10^{-7}	6.959×10^{-7}

Table B2. The CFHTLenS aperture-mass dispersion. The E mode, $\langle M_{\mathrm{ap}}^2 \rangle$, and B mode $\langle M_\times \rangle$, are given for different angular smoothing scales θ (see Section 3.5). The values of σ indicate the error from the scaled Clone covariance diagonal (Section 3.3.4). Note that for cosmological results, we do not use scales below 5 arcmin.

θ (arcmin)	$\langle M_{\mathrm{ap}}^2 \rangle(\theta)$	$\sigma[\langle M_{\mathrm{ap}}^2 \rangle(\theta)]$	$\langle M_\times^2 \rangle(\theta)$	$\sigma[\langle M_\times^2 \rangle(\theta)]$
0.9	4.640×10^{-6}	3.997×10^{-6}	5.970×10^{-6}	3.962×10^{-6}
1.1	2.615×10^{-6}	3.266×10^{-6}	5.444×10^{-6}	3.202×10^{-6}
1.4	4.631×10^{-6}	2.709×10^{-6}	2.436×10^{-6}	2.541×10^{-6}
1.7	6.978×10^{-6}	2.178×10^{-6}	3.884×10^{-7}	2.065×10^{-6}
2.2	7.939×10^{-6}	1.794×10^{-6}	1.274×10^{-7}	1.718×10^{-6}
2.7	7.842×10^{-6}	1.460×10^{-6}	-8.143×10^{-7}	1.424×10^{-6}
3.5	6.946×10^{-6}	1.191×10^{-6}	-4.514×10^{-7}	1.147×10^{-6}
4.4	6.747×10^{-6}	9.810×10^{-7}	2.530×10^{-8}	8.793×10^{-7}
5.5	6.861×10^{-6}	8.139×10^{-7}	2.168×10^{-7}	7.060×10^{-7}
6.9	6.023×10^{-6}	6.835×10^{-7}	3.835×10^{-7}	5.902×10^{-7}
8.7	5.409×10^{-6}	5.809×10^{-7}	2.212×10^{-7}	4.846×10^{-7}
11.0	4.793×10^{-6}	5.157×10^{-7}	8.553×10^{-8}	3.813×10^{-7}
13.9	3.851×10^{-6}	4.448×10^{-7}	1.480×10^{-7}	3.138×10^{-7}
17.5	3.187×10^{-6}	3.809×10^{-7}	1.037×10^{-7}	2.439×10^{-7}
22.0	2.612×10^{-6}	3.350×10^{-7}	5.001×10^{-8}	1.950×10^{-7}
27.7	2.113×10^{-6}	3.015×10^{-7}	-9.627×10^{-8}	1.619×10^{-7}
35.0	1.718×10^{-6}	2.656×10^{-7}	-7.630×10^{-10}	1.374×10^{-7}
44.1	1.269×10^{-6}	2.410×10^{-7}	1.976×10^{-7}	1.160×10^{-7}
55.5	1.002×10^{-6}	2.279×10^{-7}	1.783×10^{-7}	1.040×10^{-7}
70.0	9.834×10^{-7}	2.109×10^{-7}	1.116×10^{-7}	9.397×10^{-8}
88.2	9.004×10^{-7}	1.920×10^{-7}	8.229×10^{-8}	9.364×10^{-8}
111.1	7.437×10^{-7}	1.985×10^{-7}	8.539×10^{-8}	1.028×10^{-7}
140.0	4.320×10^{-7}	2.181×10^{-7}	1.412×10^{-7}	1.540×10^{-7}

Table B3. The CFHTLenS optimized ring statistic. The E mode, $\mathcal{R}_{\mathrm{E}}$, and B mode, $\mathcal{R}_{\mathrm{B}}$, are given for different angular smoothing scales θ (see Section 3.5). The values of σ indicate the error from the scaled Clone covariance diagonal (Section 3.3.4).

θ (arcmin)	$\mathcal{R}_{\mathrm{E}}$	$\sigma[\mathcal{R}_{\mathrm{E}}]$	$\mathcal{R}_{\mathrm{B}}$	$\sigma[\mathcal{R}_{\mathrm{E}}]$
8.7	2.405×10^{-6}	2.768×10^{-7}	2.457×10^{-8}	1.555×10^{-7}
11.1	2.012×10^{-6}	2.281×10^{-7}	7.390×10^{-9}	1.222×10^{-7}
14.2	1.919×10^{-6}	1.994×10^{-7}	3.053×10^{-8}	9.983×10^{-8}
18.2	1.662×10^{-6}	1.678×10^{-7}	1.144×10^{-8}	7.849×10^{-8}
23.3	1.449×10^{-6}	1.455×10^{-7}	3.317×10^{-8}	6.319×10^{-8}
29.9	1.174×10^{-6}	1.259×10^{-7}	4.464×10^{-8}	4.946×10^{-8}
38.2	9.886×10^{-7}	1.070×10^{-7}	2.264×10^{-8}	4.004×10^{-8}
49.0	7.827×10^{-7}	9.446×10^{-8}	1.451×10^{-9}	3.092×10^{-8}
62.7	6.077×10^{-7}	8.263×10^{-8}	3.772×10^{-8}	2.559×10^{-8}
80.3	4.535×10^{-7}	7.421×10^{-8}	3.821×10^{-8}	2.175×10^{-8}
102.8	3.844×10^{-7}	6.813×10^{-8}	4.051×10^{-8}	1.840×10^{-8}
131.6	3.154×10^{-7}	6.107×10^{-8}	4.130×10^{-8}	1.663×10^{-8}
168.6	2.728×10^{-7}	5.770×10^{-8}	2.486×10^{-8}	1.701×10^{-8}
215.8	1.906×10^{-7}	5.751×10^{-8}	3.809×10^{-8}	2.142×10^{-8}
276.4	1.338×10^{-7}	8.237×10^{-8}	3.853×10^{-8}	6.264×10^{-8}

Table B4. The COSEBIs for $\vartheta_{\min} = 10$ arcsec and $\vartheta_{\max} = 100$ arcmin. The E mode, E_n, and B mode B_n are given for the first five modes n (see Section 3.5). The values of σ indicate the error from the scaled Clone covariance diagonal (Section 3.3.4).

n	E_n	$\sigma[E_n]$	B_n	$\sigma[B_n]$
1	2.151×10^{-10}	2.748×10^{-11}	1.242×10^{-11}	1.166×10^{-11}
2	2.288×10^{-10}	4.814×10^{-11}	1.706×10^{-11}	2.195×10^{-11}
3	1.573×10^{-10}	6.157×10^{-11}	1.689×10^{-11}	3.129×10^{-11}
4	1.368×10^{-10}	6.765×10^{-11}	-8.415×10^{-12}	3.779×10^{-11}
5	1.557×10^{-10}	6.736×10^{-11}	-3.866×10^{-11}	3.971×10^{-11}

Table B5. The COSEBIs for $\vartheta_{\min} = 10$ arcsec and $\vartheta_{\max} = 250$ arcmin (see Table B4 for details).

n	E_n	$\sigma[E_n]$	B_n	$\sigma[B_n]$
1	4.841×10^{-10}	1.469×10^{-10}	9.532×10^{-11}	1.156×10^{-10}
2	3.568×10^{-10}	3.318×10^{-10}	1.729×10^{-10}	2.839×10^{-10}
3	-7.270×10^{-11}	5.712×10^{-10}	2.531×10^{-10}	5.085×10^{-10}
4	-5.526×10^{-10}	8.092×10^{-10}	2.990×10^{-10}	7.240×10^{-10}
5	-1.062×10^{-9}	9.913×10^{-10}	3.302×10^{-10}	8.724×10^{-10}

This paper has been typeset from a TeX/LaTeX file prepared by the author.